

## Investigation into the extrudability of a new Mg-Al-Zn-RE alloy with large amounts of alloying elements

Bai, Sheng Wen; Fang, Gang; Zhou, Jie

**DOI**

[10.1007/s11661-019-05242-9](https://doi.org/10.1007/s11661-019-05242-9)

**Publication date**

2019

**Document Version**

Accepted author manuscript

**Published in**

Metallurgical and Materials Transactions A: Physical Metallurgy and Materials Science

**Citation (APA)**

Bai, S. W., Fang, G., & Zhou, J. (2019). Investigation into the extrudability of a new Mg-Al-Zn-RE alloy with large amounts of alloying elements. *Metallurgical and Materials Transactions A: Physical Metallurgy and Materials Science*, 50(7), 3246-3264. <https://doi.org/10.1007/s11661-019-05242-9>

**Important note**

To cite this publication, please use the final published version (if applicable).  
Please check the document version above.

**Copyright**

Other than for strictly personal use, it is not permitted to download, forward or distribute the text or part of it, without the consent of the author(s) and/or copyright holder(s), unless the work is under an open content license such as Creative Commons.

**Takedown policy**

Please contact us and provide details if you believe this document breaches copyrights.  
We will remove access to the work immediately and investigate your claim.

1     **Investigation into the extrudability of a new Mg-Al-Zn-RE**  
2             **alloy with large amounts of alloying elements**

3                             Sheng-Wen Bai<sup>1</sup>, Gang Fang<sup>1, \*</sup>, Jie Zhou<sup>2</sup>

4     <sup>1</sup> State Key Laboratory of Tribology, Department of Mechanical Engineering, Tsinghua  
5     University, Beijing 100084, China

6     <sup>2</sup> Department of Biomechanical Engineering, Delft University of Technology, Mekelweg 2,  
7     2628 CD Delft, The Netherlands

8     \*Corresponding author, Gang Fang: Tel: +86-10-6278 2694, E-mail: [fangg@tsinghua.edu.cn](mailto:fangg@tsinghua.edu.cn)

9  
10    **Abstract**

11    The present study was aimed to determine the extrudability of a newly developed  
12    Mg-Al-Zn-RE magnesium alloy with large amounts of alloying elements. The  
13    experimental and numerical investigation clearly showed that the extrudate  
14    temperature was a crucial factor deciding if a critical temperature between 754 K and  
15    768 K (481 °C and 495 °C) was reached during extrusion, above which hot shortness  
16    occurred. Under the extrusion conditions applied, dynamic recrystallization (DRX)  
17    occurred, leading to grain refinement from a mean grain size of 165 μm in the  
18    as-solid-solution-treated billet to 8.0-10.9 μm in the extruded rods. Second-phase  
19    particles, such as Mg<sub>17</sub>Al<sub>12</sub> and Al<sub>11</sub>La<sub>3</sub>, were found to distribute on grain boundaries  
20    and aid in grain refinement. The mechanical properties of the extrudate were greatly  
21    influenced by the as-extruded microstructure and extrusion condition. As the initial

22 billet temperature decreased, the ultimate tensile strength (UTS) and elongation of the  
23 alloy increased, while yield strength (YS) remained almost unchanged. At an initial  
24 billet temperature of 523 K (250 °C), a stem speed of 3.93 mm/s and a reduction ratio  
25 of 29.8, the extruded magnesium alloy had a mean grain size of 8.0 μm. Its YS, UTS  
26 and elongation reached  $217 \pm 3$  MPa,  $397 \pm 7$  MPa and  $20 \pm 1.3\%$ , respectively.

27 **Keywords:** magnesium; extrusion; microstructure; mechanical property; hot shortness

28

## 29 **1. Introduction**

30 Since the beginning of this century, magnesium alloys, the lightest structural metallic  
31 materials, have attracted great attention for applications in 3-C (computers,  
32 communications and consumer electronics) products, automobiles and aerospace in  
33 order to realize weight reduction [1-6]. Cast magnesium alloy parts made by using a  
34 variety of casting techniques have been widely accepted for these applications [7].  
35 However, the applications of wrought magnesium alloys have been rather limited,  
36 although in general wrought magnesium alloys possess better mechanical properties  
37 than the cast counterpart and are thus more suitable for structural applications [8-9].  
38 Extruded magnesium alloy products, for example, accounted for less than 3% of the  
39 annual output of magnesium production in 2013 [10]. The limited applications of  
40 extruded products are mainly due to the low extrudability of magnesium alloys,  
41 compared to aluminum alloys, leading to low productivity and low cost-effectiveness.

42 The limited use of extruded magnesium alloy products is also due to the achievable  
43 mechanical properties that are not substantially better than those of the cast  
44 counterpart. In recent years, a lot of research efforts have been made to improve the  
45 mechanical properties and extrudability of magnesium alloys.

46

47 Basically, there are two ways to improve the mechanical properties of extruded  
48 magnesium alloys. Alloying is effective in enhancing the mechanical properties of  
49 magnesium, but at the same time imposes limitations to applicable extrusion speed, as  
50 a result of raised resistance to hot deformation, increased temperature rise during the  
51 process and lowered incipient melting point. Microstructure control throughout  
52 materials processing from casting to extrusion is also effective, especially the control  
53 of grain structure within an applicable extrusion process window by applying an  
54 optimum combination of extrusion process parameters. Obviously, it is the best if  
55 alloying and microstructure control are combined to achieve optimum mechanical  
56 properties from a refined grain structure and from the distribution of fine precipitates  
57 at a minimum loss in extrusion speed.

58

59 The effect of alloying on the microstructure, extrudability and mechanical properties  
60 of extruded magnesium alloy products depends on the amount of a chosen element  
61 and its solubility in the magnesium matrix. When its content is low, it stays dissolved  
62 in the magnesium matrix even at room temperature, creating a solid solution

63 strengthening effect. However, when the content exceeds its solubility in the  
64 magnesium matrix, second-phase particles precipitate as temperature decreases,  
65 creating a precipitation strengthening effect and possibly contributing to a refined  
66 grain structure as well by pinning grain boundaries, which in turn strengthens the  
67 alloy further. These strengthening mechanisms may operate individually or in  
68 combination. The mechanical properties of extruded magnesium were, for example,  
69 shown to be improved through the addition of Al and Zn by a combination of  
70 strengthening mechanisms, depending on the contents of these elements [11]. Yin et al.  
71 [12] found that the addition of Zn refined the grain structure of an extruded  
72 Mg-Zn-Mn alloy and led to an improved yield strength. In Mg-5Sn- $x$ Zn alloys ( $x=1,$   
73 2, 4), the amounts of Mg<sub>2</sub>Sn and MgZn particles increased with increasing Zn content,  
74 which contributed to the mechanical properties of the extruded magnesium alloys  
75 through precipitation strengthening [13]. Small amounts of Ca were found to be able  
76 to refine the grain structure and improve both the tensile strength and elongation of  
77 Mg-Al-Zn and Mg-Zn alloys [14, 15]. Rare earth (RE) elements, such as Gd, Y and  
78 Ce, were added to different extruded magnesium alloys to enhance their mechanical  
79 properties [16-21]. For example, Y improved the mechanical properties of Mg-Zn-Zr  
80 alloys through grain refinement and the formation of the I-phase (Mg<sub>3</sub>Zn<sub>6</sub>Y).  
81 However, an excessive addition of Y to the alloys led to the formation of the W-phase  
82 (Mg<sub>3</sub>Zn<sub>3</sub>Y<sub>2</sub>), which decreased the strengths. Actually, it is the ratio of Y to Zn (wt. %)  
83 that determines the volume fraction of the I-phase and its strengthening effect [18].

84 Zeng et al. [22] also demonstrated that the polygon-shaped  $Mg_3Zn_6Y$  phase played an  
85 important role in strengthening the extruded magnesium alloy Mg-6Zn-1.5Y-0.5Zr.  
86 Stanford et al. [23] found that the strength of magnesium was greatly improved by  
87 adding 0.22-4.65% Gd, owing to the mechanisms of recrystallized grain refinement  
88 and solution strengthening. Zhang et al. [24] revealed that the synthetic additions of  
89 Ca, Ce and La to the Mg-6.0Zn alloy resulted in the refinement of secondary phases  
90 and precipitates, promoting the pinning effect to restrict grain growth and the  
91 dispersion strengthening effect. Homma et al. [25] developed a high-strength  
92 magnesium alloy Mg-1.8Gd-1.8Y-0.7Zn-0.2Zr with an ultimate tensile strength (UTS)  
93 of 542 MPa and a 0.2% proof stress of 473 MPa. The high strengths were achieved  
94 thanks to fine precipitates formed during aging subsequent to hot extrusion. Yamasaki  
95 et al. [26] found that the yield strength of the warm-extruded magnesium alloy  
96 Mg-Zn-2.5Gd reached a high level of 345 MPa, because of the refinement of grains  
97 and the dispersion of a precipitate with a long period ordered (LPO) structure. Chen et  
98 al. [27] investigated the effect of Nd addition on the microstructures and mechanical  
99 properties of the Mg-6Al-2Ca-xNd ( $x=0, 1, 2, 3, 4$  and 5 wt.%) alloys. With  
100 increasing content of Nd, the amounts of  $Al_2Nd$  and  $Al_3Nd$  phases increased, while  
101 the amount of  $Mg_{17}Al_{12}$  decreased. The presence of the Al-Nd compounds contributed  
102 to the refinement of the recrystallized grain structure formed during hot extrusion,  
103 leading to an enhanced yield strength. Therefore, it is critically important to

104 understand the strengthening phase formed in RE-containing magnesium alloys and  
105 its sizes, volume fraction and distribution.

106

107 On the other hand, as mentioned earlier, with the addition of alloying elements to  
108 magnesium, the extrudability usually decreases [11]. Luo et al. [28], for example,  
109 found that the incipient melting point of the magnesium alloy AZ31 was 371 K (98 °C)  
110 lower than that of AM30 due to the presence of Zn in the former. It means that AZ31  
111 is more susceptible to hot shortness. To prevent hot shortness from occurring, a lower  
112 initial billet temperature must be considered, if extrusion speed and reduction ratio are  
113 desired to be fixed. As a result, the extrusion pressure required for the process will be  
114 higher. If the force capacity of the available extrusion press is not enough, extrusion  
115 speed or reduction ratio must be reduced in order to lower the pressure requirement,  
116 leading to sacrifice in extrusion productivity. In the case of high-strength magnesium  
117 alloys with large amounts of alloying elements, more severe limitations are imposed  
118 on the applicable extrusion conditions. For each alloy, its extrusion window must be  
119 specifically defined in order to avoid hot shortness and achieve the highest possible  
120 extrusion productivity in combination with the consideration on the microstructure  
121 and mechanical properties desired to achieve.

122

123 During hot extrusion, the main process parameters, i.e., initial billet temperature,  
124 extrusion speed and reduction ratio, may all influence the microstructure of an

125 extruded magnesium alloy. The mechanical properties of the alloy depend on its  
126 microstructural characteristics, such as grain size, the intensity of texture and the  
127 distribution of second-phase particles [29-33]. Murai et al. [29] found that fine grains  
128 in the extruded magnesium alloy AZ31 were obtained at a low initial billet  
129 temperature and a low extrusion speed, resulting in high mechanical properties of the  
130 extrudate. Ishihara et al. [30] reported that at a given initial billet temperature of 693  
131 K (420 °C) and extrusion speed of 5 m/min, the mean grain size of the extruded  
132 magnesium alloy AZ31 increased from 30 to 170  $\mu\text{m}$ , when reduction ratio was  
133 increased from 10 to 100. Zhang et al. [31] investigated the effect of the initial billet  
134 temperature on the microstructure and mechanical properties of the extruded  
135 Mg-1.0Zn-0.5Ca alloy. They found that with decreasing initial billet temperature from  
136 673 K to 603 K (400 °C to 330 °C), the mean grain size decreased from 25 to 2.5  $\mu\text{m}$   
137 and the ultimate tensile strength (UTS) increased from 201 to 300 MPa. Tong et al.  
138 [32] found that the basal texture of the Mg-5.3Zn-0.6Ca alloy was weakened at a  
139 higher extrusion speed, which resulted in a lower tensile yield strength. Park et al. [33]  
140 demonstrated that the temperature rise occurring during extrusion increased the  
141 solubility of Sn in the magnesium matrix and thereby reduced the volume fraction of  
142  $\text{Mg}_2\text{Sn}$  precipitates in the Mg-Sn-Al-Zn extrudate, resulting in a low strength.  
143 Therefore, the choice of extrusion parameters is of critical importance for the  
144 achievable mechanical properties of an extruded magnesium alloy.

145

146 Indeed, many of recent research efforts have aimed at achieving the highest possible  
147 strength through optimizing extrusion condition, often in combination with  
148 modification of alloy composition. By performing extrusion at an extrusion ratio of 44,  
149 a ram speed of 60 mm/min and billet temperature of 623 K (350 °C), for example,  
150 Shahzad et al. [34] obtained the ultimate tensile strength (UTS) of 328 MPa for the  
151 magnesium alloy AZ80. Chen et al. [35] found that the UTS of the extruded  
152 magnesium alloy Mg-5.3Zn-1.13Nd-0.51La-0.28Pr-0.79Zr could reach 325-350 MPa,  
153 when the billet temperature applied was 523 K (250 °C). Singh et al. [36] developed  
154 the extruded magnesium alloys Mg-6xZn-xY ( $x=0.2, 0.35$  and  $0.5$  at. %) with UTS  
155 varying from 397.8 to 418.6 MPa and elongation values over 12%. Park et al. [37]  
156 reported that the UTS of the Mg-9Al-0.6Zn alloy reached 375 MPa after extrusion at a  
157 billet temperature of 523 K (250 °C), extrusion speed of 1 mm/s and a reduction ratio of  
158 7.35. Bu et al. [38] developed a new magnesium alloy containing large amounts of  
159 alloying elements, including La and Gd (Mg-Al-Zn-RE). The effects of La and Gd on  
160 the microstructure and mechanical properties of the extruded alloy were extensively  
161 investigated. The results showed that, as a result of La and Gd additions, the  $Al_{11}La_3$ ,  
162  $Al_8Mn_4Gd$  and  $Al_3Gd$  phases were present in the extruded alloy in addition to the  
163  $Mg_{17}Al_{12}$  phase. During extrusion, particle stimulated nucleation (PSN) occurred due to  
164 the presence of abundant second-phase particles, leading to the formation of fine,  
165 recrystallized grains. The alloy had a UTS of 397 MPa, being higher than that of the  
166 traditional magnesium alloy AZ80, owing to a combination of grain refinement

167 strengthening, precipitation strengthening, solid-solution strengthening, dislocation  
168 strengthening and subgrain strengthening. Therefore, the alloy was considered to be  
169 highly promising for aircraft applications. However, the effects of extrusion process  
170 parameters on the microstructure and mechanical properties of the alloy were not  
171 investigated. As microstructural changes, such as dynamic recrystallization and  
172 precipitation, are largely governed by the local thermomechanical conditions during  
173 hot extrusion, it was hypothesized that the as-extruded microstructure and resultant  
174 mechanical properties, especially elongation (10%) [38], would be optimized through  
175 optimizing the extrusion condition.

176

177 The present work concerned a case study on the extrudability, microstructure evolution  
178 during extrusion and the resulting mechanical properties of the newly developed  
179 magnesium alloy Mg-Al-Zn-RE. It was intended to serve as an example to show how to  
180 determine the extrudability of a new magnesium alloy and understand the effect of  
181 extrusion condition on its microstructure and mechanical properties through a  
182 combination of experimental research and numerical simulation using the finite  
183 element (FE) method. The extrusion experiments were performed by using a  
184 tailor-designed die setup. Different combinations of extrusion parameters, namely  
185 initial billet temperature, extrusion speed and reduction ratio, were employed. FE  
186 simulations of hot extrusion were carried out to predict the extrudate temperature that  
187 was hard to measure accurately in real extrusion operation. In addition, the effects of

188 extrusion parameters on the microstructure evolution and mechanical properties of the  
189 alloy were investigated through microstructure observation and tensile tests of the  
190 extrudate.

191

## 192 **2. Material, extrusion experiments and numerical simulations**

### 193 **2.1 Material**

194 The nominal chemical composition of the newly developed Mg-Al-Zn-RE alloy is  
195 given in Table 1. The alloy was designed on the basis of AZ81 [38], which is known  
196 for having a very narrow range of applicable deformation conditions [39]. The  
197 addition of the rare earth elements (i.e., La and Gd) tended to lower its workability  
198 further. Hot compression tests indeed showed that this alloy was extraordinarily prone  
199 to hot shortness; hot cracking occurred at temperatures higher than 693 K (420 °C).  
200 To push the temperature limit upwards, the as-cast alloy was solid-solution-treated at  
201 693 K (420 °C) for 24 h, following by water quenching, in order to dissolve  
202 second-phase particles, such as  $Mg_{17}Al_{12}$  that has an incipient melting point of 710 K  
203 (437 °C) [40]. The solution treatment was also intended to homogenize the as-cast  
204 microstructure and improve its extrudability. Cylindrical billets with a diameter of 29  
205 mm and lengths of 23 and 15 mm were prepared for extrusion experiments.

206 Table 1. Chemical composition (wt. %) of the Mg-Al-Zn-RE alloy.

Element	Al	Zn	Mn	La	Gd	Mg
---------	----	----	----	----	----	----

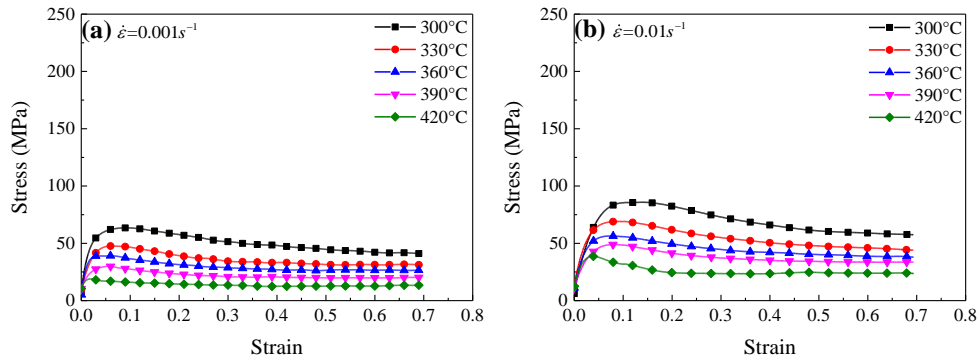
Chemical composition (wt. %)	8.0~8.8	0.3~0.8	0.15~0.3	0.7~1.3	0.3~0.7	Bal.
------------------------------	---------	---------	----------	---------	---------	------

207

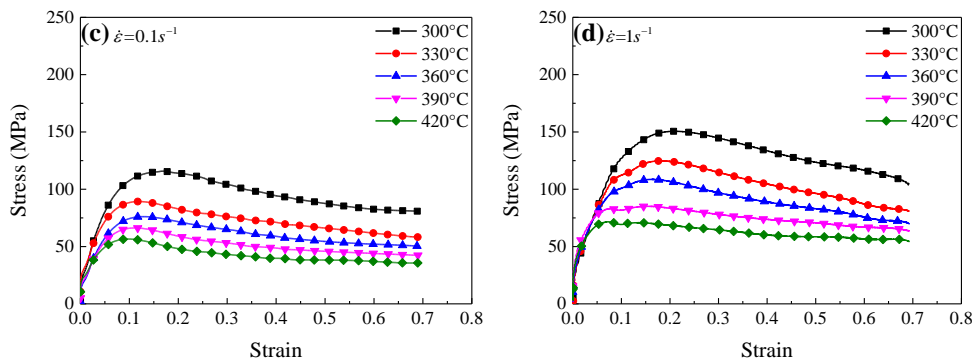
## 208 2.2 Hot compression tests

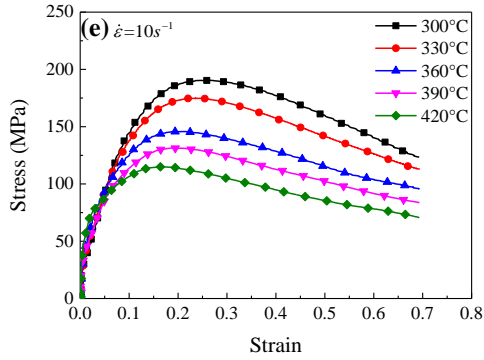
209 A constitutive model of the magnesium alloy is needed for the FE simulations of  
 210 extrusion. To determine the constitutive constants, uniaxial compression tests of  
 211 cylindrical specimens with sizes of  $\phi 8 \times 12$  mm were performed by using a Gleeble  
 212 1500 thermomechanical simulator. Test temperatures from 573 K to 693 K (300 °C to  
 213 420 °C) and with an interval of 30 K (30 °C) were chosen. Strain rates selected were  
 214 0.001, 0.01, 0.1, 1 and  $10 \text{ s}^{-1}$ . The flow stress-strain curves obtained at different  
 215 temperatures and strain rates are shown in Fig. 1. The hyperbolic sine-type equation  
 216 (Eq. 1), proposed by Sellars and McTegart [41], was adopted to describe the  
 217 deformation behavior of the material.

218



219





220

221 Fig. 1. Flow stress-strain curves of the magnesium alloy at temperatures from 573 K to  
 222 693 K (300 °C to 420 °C) and strain rates (a) 0.001 s<sup>-1</sup>, (b) 0.01 s<sup>-1</sup>, (c) 0.1 s<sup>-1</sup>, (d) 1 s<sup>-1</sup>  
 223 and (e) 10 s<sup>-1</sup>.

224 
$$\dot{\varepsilon} = A[\sinh(\alpha\sigma)]^n \exp\left(\frac{-Q}{RT}\right) \quad (1)$$

225 where,  $A$ ,  $\alpha$  and  $n$  are material constants,  $Q$  is the activation energy for hot

226 deformation, and  $R$  is the gas constant. The constitutive constants obtained were used

227 as material constants in the model for the FE simulations of extrusion (Table 2).

228

229 Table 2. Constitutive constants of the magnesium alloy (Mg-Al-Zn-RE).

Constitutive constant	$A$	$\alpha$	$n$	$Q$ (kJ/mol)
Value	2.3188e+10	1.721e-2	4.5164	141.329

230

### 231 2.3 Extrusion tooling setup

232 The tooling setup, specially designed for this research, consisted of a structural

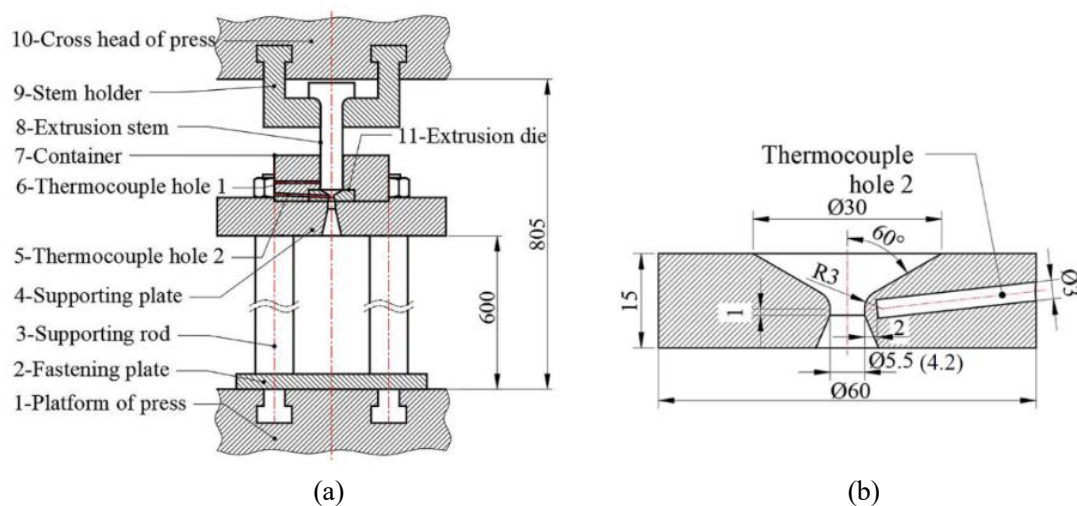
233 supporting framework, a heating system, a die with a round opening, a container, a

234 stem and a stem holder (Fig. 2). The supporting framework included a fastening plate,

235 supporting rods and a supporting plate, which were used to fix the die setup on the

236 platform of a press driven by a hydraulic system. The stem holder was connected to

237 the crosshead of the hydraulic press. Four resistance-heating elements with a total  
 238 power of 2000 W were employed to heat the container, extrusion die and billet.  
 239 Heating was controlled by a PID (Proportion Integration Differentiation) controller  
 240 based on the feedback temperature measured by Thermocouple 1. Thermocouple 2  
 241 was inserted into the die to measure the temperature near the die orifice during  
 242 extrusion. The measuring point was 2 mm away from the die bearing (Fig. 2b).  
 243  
 244 Two extrusion dies with orifice diameters of 5.5 and 4.2 mm were employed for  
 245 extrusion at reduction ratios of 29.8 and 51.0, respectively, while the diameter of the  
 246 container liner stayed unchanged (30 mm). For each die, the inlet angle was 60° and  
 247 the length of straight die bearing was 1 mm.



248  
 249 (a)  
 250 (b)  
 Fig. 2. Tooling set-up to extrude rods: (a) schematic and (b) dimensions of one of the extrusion dies.

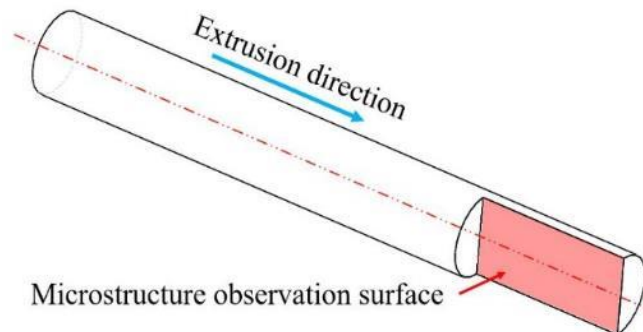
## 251 **2.4 Extrusion experiments**

252 Extrusion experiments were performed by using the tooling setup mounted on a  
253 hydraulic press with a force capacity of 2 MN. Before extrusion, the billet was heated  
254 to a preset temperature at a rate of 8 K/min (8 °C/min) and soaked for 15 min. The  
255 container and die were heated to the same temperature as the billet. During extrusion,  
256 the temperature near the die orifice was measured by Thermocouple 2. After extrusion,  
257 the extruded rod was cut off from the discard and air-cooled. Initial billet temperature,  
258 extrusion speed and reduction ratio were taken as the main process variables. Initial  
259 billet temperature was set at 523, 573, 623, 673 and 713 K (250, 300, 350, 400 and  
260 440 °C). Stem speed increased from 0.48 mm/s to 8.24 mm/s. Reduction ratios were  
261 29.8 and 51.0, as mentioned in Subsection 2.3.

## 262 **2.5 Microstructure observation**

263 Samples were cut from the extruded rods along the longitudinal extrusion direction  
264 (Fig. 3). The exposed surfaces were ground and mechanically polished. An etchant  
265 composed of 5 g picric acid, 10 ml acetic acid, 10 ml deionized water and 100 ml  
266 absolute ethyl alcohol was used to etch the samples. The microstructures of the  
267 samples were observed using an optical microscope (Zeiss Axio Scope.A1) and a  
268 scanning electron microscope (SEM, FEI Quanta 200 FEG) equipped with an energy  
269 dispersive x-ray spectroscope (EDS). The grain sizes of the extrudate were  
270 determined by using the linear intercept method. The sizes and volume fractions of

271 second-phase particles were measured by using the commercial software Image-Pro  
272 Plus on the basis of SEM micrographs.



273

274 Fig. 3. Schematic of the longitudinal section of an extruded rod for microstructure observation.

## 275 2.6 Tensile tests

276 Tensile specimens were prepared by machining from the extruded rods. They had a  
277 total length of 90 mm, a gauge length of 25 mm and a gauge diameter of 4 mm,  
278 conforming to the standard GB/T 228.1-2010. Tensile tests were conducted using a  
279 universal material testing machine (AG-X, Shimadzu) at a crosshead speed of 1  
280 mm/min. Tensile force was applied in the direction being the same as the extrusion  
281 direction. The test of the specimen processed under each condition was repeated at  
282 least twice to ensure the reproducibility of the data.

283

## 284 2.7 Finite element simulations

285 FE simulations were performed to predict the temperature of the extrudate at the die  
286 orifice, as affected by the extrusion variables. An axisymmetric FE model (Fig. 4) was

287 built by using the commercial software package DEFORM. The billet, extrusion die,  
 288 stem and container were all meshed to be composed of quadrilateral elements. The  
 289 billet was defined as a thermo-rigid-plastic material, and the thermomechanical effect  
 290 occurring during extrusion was taken into account. The extrusion tools were  
 291 considered to be rigid objects and heat transfer was allowed. The constitutive equation  
 292 (Eq. 1) was applied in the FE simulations. The initial temperatures of the container  
 293 and die were set to be the same as those used in the extrusion experiments, while the  
 294 stem was set at an initial temperature of 293 K (20 °C). Heat exchanges between the  
 295 billet, extrusion tooling and surrounding environment were taken into consideration. A  
 296 shear friction model was adopted at the interfaces between the billet and extrusion  
 297 tooling and the friction coefficient was set at 1.0 [42]. The physical properties of the  
 298 magnesium alloy and tooling material (H13 tool steel) are listed in Table 3 [43].

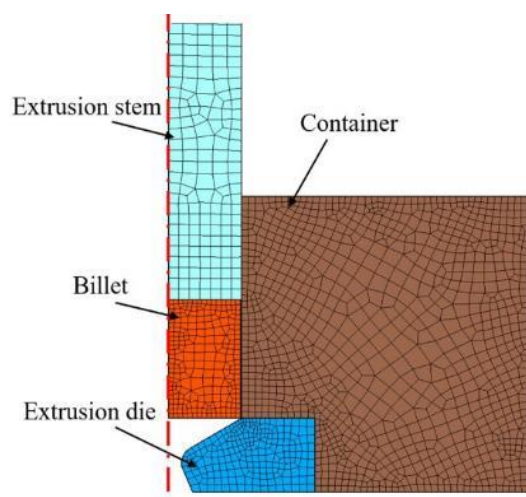


Fig. 4. Axisymmetric FE model to simulate the extrusion process to produce rods.

Table 3. Physical properties of the billet and extrusion tooling.

Physical property	Magnesium alloy	H13 tool steel
-------------------	-----------------	----------------

Thermal conductivity (W/(m °C))	96	28.4
Heat capacity (N/(mm <sup>2</sup> °C))	2.097 at 600 K (327°C)	5.6
	2.275 at 800 K (527°C)	
Heat transfer coefficient between tooling and workpiece (N/(°C s mm <sup>2</sup> ))	11	11
Heat transfer coefficient between tooling/workpiece and air (N/(°C s mm <sup>2</sup> ))	0.02	0.02
Emissivity	0.7	0.7

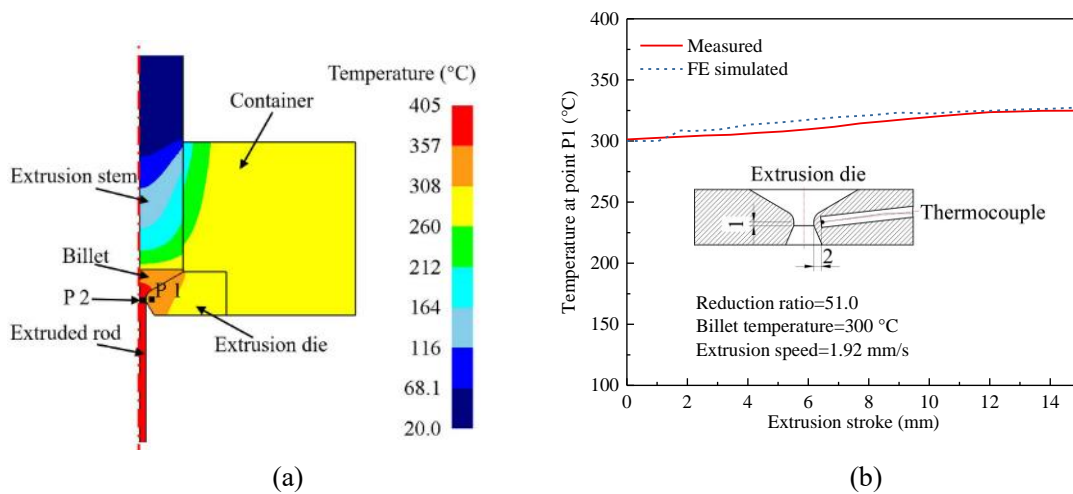
---

### 302 **3. Results and discussion**

#### 303 **3.1 Extrudate temperature**

304 The extrudate temperature at the die exit, the most important process parameter that  
305 strongly influences the surface quality and microstructure of the extrudate, depends on  
306 the initial billet temperature, extrusion speed and reduction ratio. It is however  
307 difficult to measure directly and accurately. To verify the extrudate temperature  
308 predicted from FE simulations, comparisons with the temperatures near the die  
309 bearing, measured by inserted Thermocouple 2, were made. Fig. 5a shows an example  
310 of the predicted temperature distribution inside the extruded billet, rod, and extrusion  
311 tooling, when the initial billet temperature was 573 K (300 °C), reduction ratio 51.0  
312 and stem speed 1.92 mm/s. The temperature predicted at point P1 inside the die  
313 reached a peak value of 600 K (327 °C) at a stem displacement of 15 mm. It was very  
314 close to the value of 598 K (325 °C) measured by Thermocouple 2. In addition, the  
315 calculated and measured temperature evolutions at point P1 during extrusion were

316 compared. The results (Fig. 5b) showed that the simulated temperatures were in  
 317 agreement with the experimentally measured values. The differences between  
 318 simulated and measured temperatures were negligible. It indicated that the present FE  
 319 model of extrusion was reliable in temperature calculation. Based on this fact, we  
 320 considered the calculated temperature at point P2 to be the exact temperature of the  
 321 extrudate surface. In addition, a large difference in temperature between the extrudate  
 322 surface (678 K, i.e., 405 °C at point P2) and measuring point (600 K, i.e., 327 °C at  
 323 point P1) was found, even though there was a distance of only 2 mm between these  
 324 two points. It confirmed that the measured die temperature could not be used as the  
 325 temperature of the extrudate directly.



326  
 327

328 Fig. 5. Predicted temperature distribution inside the billet, extrudate and extrusion tooling (a) and  
 329 comparison between the measured and predicted temperatures at P1 along with stem displacement

330  
 331

(b).

332 Fig. 6 shows the FE simulated temperature evolutions at point P2 under different  
333 extrusion conditions. At the initial stage of extrusion, the temperature at point P2 rose  
334 significantly, which was attributed to heat generation from both plastic deformation  
335 and severe friction between the billet and tooling. The temperature rise due to  
336 deformation heating can be described by using Eq. 2, where  $\eta$  is the adiabatic factor  
337 with a value between 0.9 and 0.95, and  $\rho$  is the specific density and  $C_p$  is the specific  
338 heat [44].

$$339 \quad \Delta T = \frac{\eta \int \sigma d\varepsilon}{\rho C_p} \quad (2)$$

340

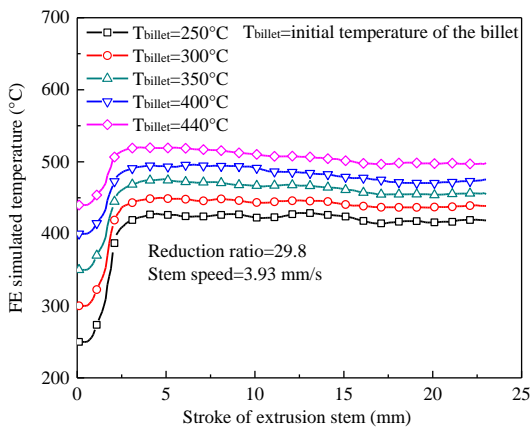
341 Eq. 3 gives the shear-type friction model employed during the simulations, where  $\tau$  is  
342 the shear stress, and  $m$  is the friction factor [45]. The friction factor was set to be 1,  
343 considering the severe friction between the tooling and billet [42]. The frictional  
344 heating contributed to temperature rise during the extrusion process. In the meantime,  
345 heat was transferred between the billet and tooling and dissipated into the atmosphere.  
346 With rising extrudate temperature, more heat was transferred from the extrudate to the  
347 tooling. Heat generation and dissipation to the die competed with each other, and then  
348 the extrudate temperature reached a steady state.

$$349 \quad \tau = \frac{m\sigma}{\sqrt{3}} \quad (3)$$

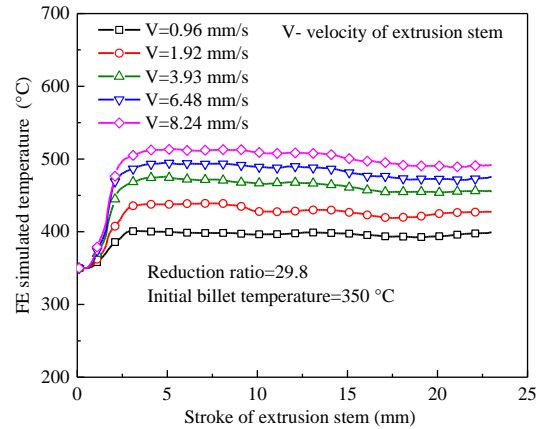
350 Fig. 7 shows the simulated temperatures at point P2, when two different friction factor  
351 values of 0 and 1 were applied. The same reduction ratio of 29.8, extrusion speed of

352 3.93 mm/s and initial billet temperature 523 K (250 °C) were employed in these  
 353 simulations. When the fraction factor values were 0 and 1, the temperature increments  
 354 of extrudate were 124 K and 179 K (124 °C and 179 °C), respectively. The result was  
 355 consistent with the above statement that the temperature increment during extrusion  
 356 was partially attributed to the heat generation from severe friction between the billet  
 357 and tooling.

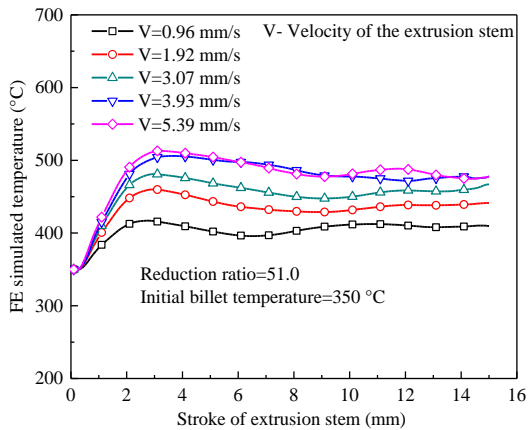
358  
 359  
 360  
 361



(a)



(b)



(c)

362

363

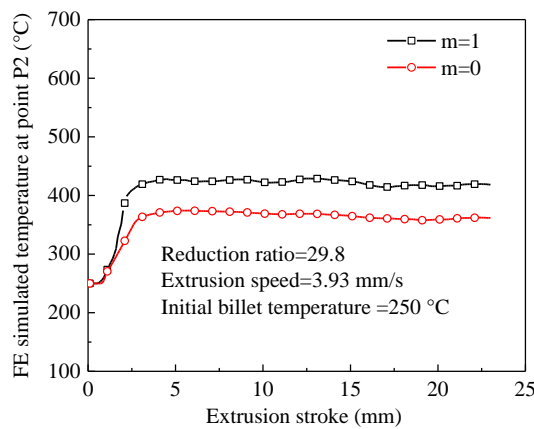
364

365

366 Fig. 6. FE simulated temperature evolutions at point P2 during extrusion: (a) at a reduction ratio of  
 367 29.8, stem speed of 3.93 mm/s and different initial billet temperatures, (b) at a reduction ratio of  
 368 29.8, initial billet temperature of 623 K (350 °C) and different stem speeds, and (c) at a reduction  
 369 ratio of 51.0, initial billet temperature of 623 K (350 °C) and different stem speeds.

370

371



372

373

Fig. 7. Simulated temperatures at point P2 with friction factor values of 0 and 1.

374

375 When reduction ratio was 29.8 and stem speed 3.93 mm/s, the maximum extrudate  
 376 temperatures reached 702, 723, 749 769 and 793 K (429, 450, 476, 496 and 520 °C)  
 377 during extrusion at initial temperatures of 523, 573, 623, 673 and 713 K (250, 300,  
 378 350, 400 and 440 °C), respectively (Fig. 6a), meaning temperature increments of 179,  
 379 150, 126, 96 and 80 K (179, 150, 126, 96 and 80 °C), respectively. As the initial billet  
 380 temperature increased, the temperature increment during extrusion decreased. This  
 381 can be explained by the fact that the lower the initial billet temperature, the more heat  
 382 generation from the higher flow stress of the magnesium alloy.

383

384 Fig. 6b shows the temperature evolutions at a reduction ratio of 29.8, initial billet  
385 temperature of 623 K (350 °C) and stem speeds of 0.96, 1.92, 3.93, 6.48 and 8.24  
386 mm/s. The maximum temperature increments were 61, 89, 126, 145 and 154 K (61,  
387 89, 126, 145 and 154 °C), respectively. With increasing extrusion speed, the  
388 maximum temperature of the extrudate grew. There are two factors that lead to the  
389 increases in extrudate temperature. On the one hand, the enhanced flow stress of the  
390 billet material at a higher extrusion speed leads to more heat generation than that at a  
391 lower extrusion speed. On the other hand, heat generation at a higher extrusion speed  
392 is less dissipated to the die.

393

394 When reduction ratio increased to 51.0 and the initial billet temperature remained  
395 unchanged (623 K, i.e., 350 °C), the maximum temperature increments were 67, 110,  
396 131, 206 and 213 K (67, 110, 131, 206 and 213 °C), at stem speeds of 0.96, 1.92, 3.07,  
397 3.93 and 5.39 mm/s, respectively (Fig. 6c). Comparison between the extrudate  
398 temperatures at these two reduction ratios (Fig. 6b and c) showed that a larger  
399 temperature increment appeared at a higher reduction ratio, but at the same initial  
400 billet temperature and extrusion speed. It can be explained by the fact that a higher  
401 strain rate at a larger reduction ratio contributes to the temperature increase of the  
402 extrudate.

403

### 404 3.2 Surface quality

405 The surface quality of an extruded magnesium alloy rod is negatively influenced by  
406 the defect of hot shortness. In general, the tendency for hot shortness to occur  
407 increases with increasing initial billet temperature, reduction ratio and extrusion speed.  
408 It is caused by an excessively high temperature due to heat generation inside the  
409 magnesium alloy undergoing large plastic deformation during extrusion. Figs. 8-10  
410 show three groups of extruded magnesium alloy rods, which are arranged in a  
411 convenient way to demonstrate the influences of the initial billet temperature,  
412 extrusion speed and reduction ratio on the surface quality of the extruded rods.

413

414 Fig. 8 shows the magnesium alloy rods extruded at a reduction ratio of 29.8, stem  
415 speed of 3.93 mm/s and different initial billet temperatures. Defect-free surfaces of  
416 the extruded rods were obtained, when the initial billet temperatures were lower than  
417 673 K (400 °C) (Fig. 8a-c). When the initial billet temperature increased to 673 K  
418 (400 °C), however, hot shortness occurred on the surface of the extruded rod (Fig. 8d).  
419 With a further increase in initial billet temperature to 713 K (440 °C), large and deep  
420 cracks on the surface of the extruded rod became visible to the naked eye (Fig. 8e).  
421 For the rods extruded under these conditions, FE simulation predicted the maximum  
422 extrudate temperatures  $T_e$  of 769 K and 793 K (496 °C and 520 °C). It could be  
423 inferred that the critical temperature for hot shortness to occur lay from 749 K to 769  
424 K (476 °C to 496 °C). It was thus the initial billet temperature that influenced the

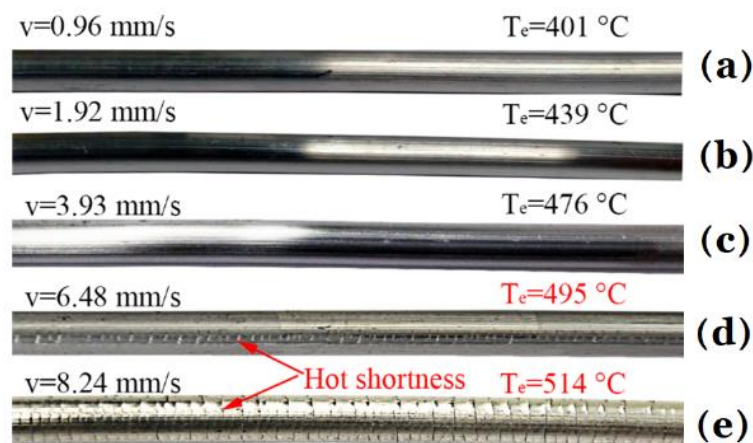
425 surface quality of the extrudate [46, 47]. At the die bearing, tensile stresses due to  
 426 severe friction exceeded the tensile strength of the material at the surface and  
 427 consequently tearing occurred (Fig. 8d). If the heat generated from friction and hot  
 428 deformation led to further temperature increases at the die bearing to the incipient  
 429 melting point, localized melting took place, which would cause severe cracking on the  
 430 surface (Fig. 8e).



431  
 432 Fig. 8. Magnesium alloy rods extruded at a reduction ratio of 29.8, stem speed of 3.93 mm/s and  
 433 different billet temperatures.  $T_e$  is the maximum extrudate temperature. (a)  $T=523$  K (250 °C) and  
 434  $T_e=702$  K (429 °C); (b)  $T=573$  K (300 °C) and  $T_e=723$  K (450 °C); (c)  $T=623$  K (350 °C) and  
 435  $T_e=749$  K (476 °C); (d)  $T=673$  K (400 °C) and  $T_e=769$  K (496 °C); (e)  $T=713$  K (440 °C) and  
 436  $T_e=793$  K (520 °C).

437 Extrusion speed is another factor influencing the surface quality of the extrudate,  
 438 which embodies heat generation and dissipation during extrusion. It is obvious that  
 439 heat generation increases with increasing extrusion speed, because a higher strain rate  
 440 corresponds to more dynamic plastic deformation, and less heat is dissipated to the

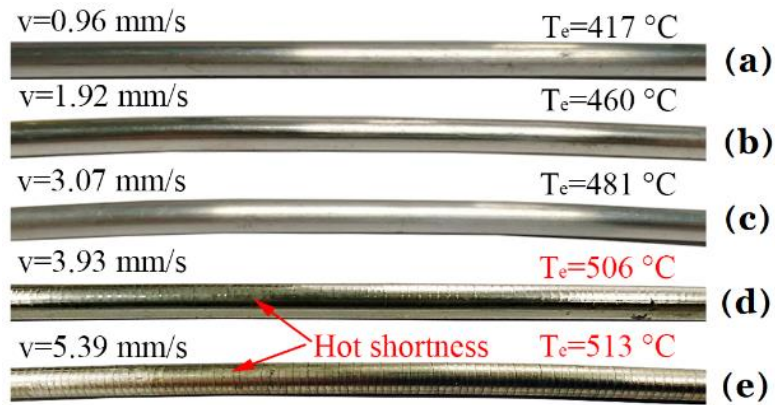
441 surrounding as a result of shortened process time, as shown in Fig. 6b. It is the raised  
 442 extrudate temperature that limits the applicable extrusion speed. In the present  
 443 research, at the same initial billet temperature of 623 K (350 °C) and reduction ratio  
 444 of 29.8, the rods extruded at different stem speeds had different surface features (Fig.  
 445 9). When stem speeds were lower than 3.93 mm/s, the extruded magnesium alloy rods  
 446 had smooth surface finish (Fig. 9a-c). When stem speed increased to 6.48 mm/s,  
 447 however, minor cracks appeared on the surface of the extruded rod (Fig. 9d). Severe  
 448 hot shortness occurred at the stem speed of 8.24 mm/s (Fig. 9e). FE simulations  
 449 indicated the extrudate surface temperatures of 749, 768 and 787 K (476, 495 and  
 450 514 °C), at stem speeds of 3.93, 6.48 and 8.24 mm/s, respectively (Fig. 6b). In  
 451 combination with the results shown earlier in Fig. 8d, the critical temperature for hot  
 452 shortness to occur would be in the range of 749 K and 768 K (476 °C and 495 °C).



453  
 454 Fig. 9. Magnesium alloy rods extruded at a reduction ratio of 29.8, initial billet temperature of 623  
 455 K (350 °C) and different stem speeds. (a)  $v = 0.96$  mm/s and  $T_e = 674$  K (401 °C); (b)  $v = 1.92$  mm/s

456 and  $T_e=712$  K (439 °C); (c)  $v=3.93$  mm/s and  $T_e=749$  K (476 °C); (d)  $v=6.48$  mm/s and  $T_e=768$  K  
457 (495 °C); (e)  $v=8.24$  mm/s and  $T_e=787$  K (514 °C).  $T_e$  is the maximum extrudate temperature.

458 As mentioned earlier, heat generated from the plastic deformation of the billet  
459 material leads to the temperature rise of the extrudate. Reduction ratio is a process  
460 parameter that is directly related to the amount of plastic deformation. The extrusion  
461 experiments performed at a higher reduction ratio of 51.0 clearly depicted the effect  
462 of reduction ratio on extrudate surface quality (compare Fig. 10 and Fig. 9). When  
463 reduction ratio was 51.0, initial billet temperature 623 K (350 °C) and stem speed  
464 3.93 mm/s, the maximum extrudate temperature reached 779 K (506 °C) and hot  
465 shortness occurred. At the lower reduction ratio of 29.8, however, the extrudate  
466 exhibited sound surface (Fig. 9c) and under this extrusion condition the maximum  
467 extrudate temperature was only 749 K (476 °C). It clearly indicated that the high  
468 reduction ratio increased the tendency of hot shortness. Fig. 10c shows the good  
469 surface of the extrudate at a stem speed of 3.07 mm/s and under this extrusion  
470 condition the extrudate temperature was 754 K (481 °C). By combining the results  
471 shown in Figs. 8, 9 and 10, one may infer the critical temperature for hot shortness to  
472 occur to be in the range of 754 K and 768 K (481 °C to 495 °C). The extrudate  
473 temperature of 754 K (481 °C) can be taken as a conservative critical temperature to  
474 avoid hot shortness.



475

476 Fig. 10. Magnesium alloy rods extruded at a reduction ratio of 51.0, initial billet temperature of

477 623 K (350 °C) and different stem speeds. (a)  $v=0.96$  mm/s and  $T_e=987$  K (417 °C); (b)  $v=1.92$

478 mm/s and  $T_e=733$  K (460 °C); (c)  $v=3.07$  mm/s and  $T_e=754$  K (481 °C); (d)  $v=3.93$  mm/s and

479  $T_e=779$  K (506 °C); (e)  $v=5.39$  mm/s and  $T_e=786$  K (513 °C).  $T_e$  is the maximum extrudate

480 temperature.

481

482

### 483 3.3 Microstructures

484 Fig. 11 shows the microstructures of the as-cast and the as-solid-solution-treated

485 Mg-Al-Zn-RE alloy. The as-cast alloy had a dendritic magnesium matrix and

486 interdendritic second-phase particles (Fig. 11a). Morphology and composition

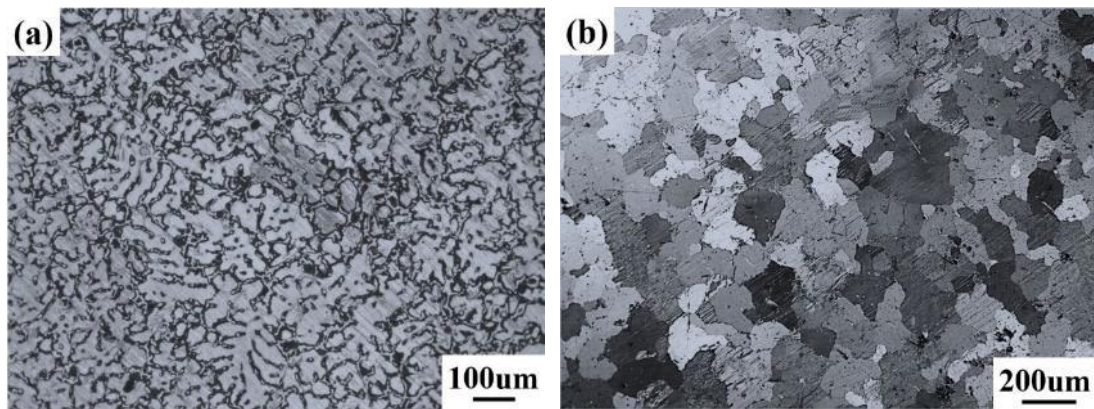
487 analyses indicated the presence of four kinds of second-phase particles in the as-cast

488 alloy, namely reticulate phase  $Mg_{17}Al_{12}$ , needle-like or lamellar phase  $Al_{11}La_3$ , and

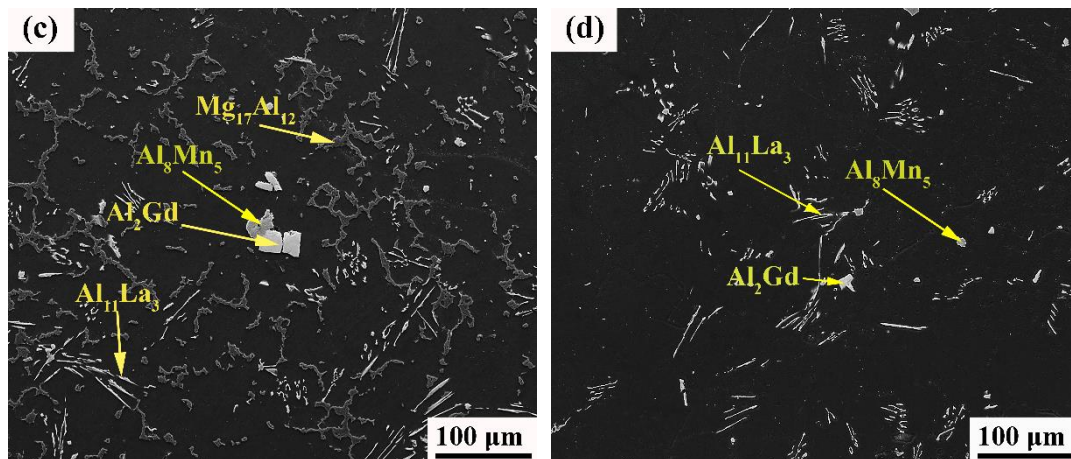
489 block-shaped phases  $Al_8Mn_5$  and  $Al_2Gd$  (Figs. 11c, e-h and Table 4).  $Mg_{17}Al_{12}$  and

490  $Al_8Mn_5$  were the common intermetallic compounds in commercial Mg-Al-Zn alloys

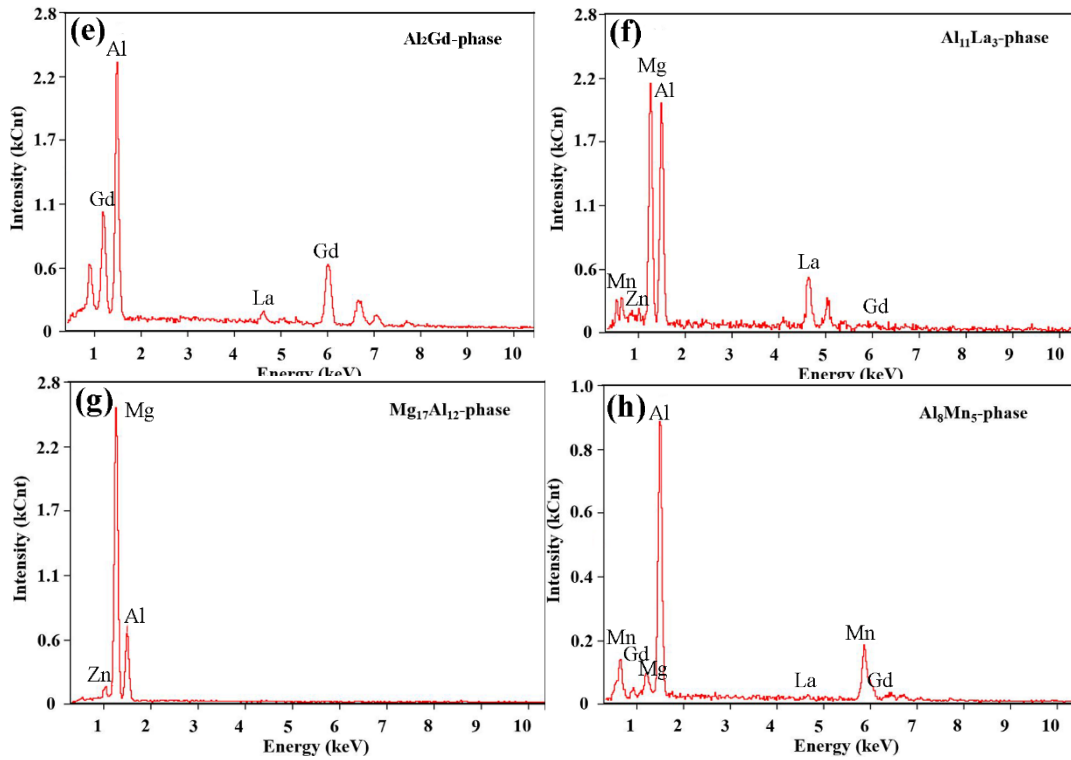
491 with a high Al content [48, 49].  $\text{Al}_{11}\text{La}_3$  and  $\text{Al}_2\text{Gd}$  were the compounds whose  
492 formation was due to the addition of rare earth elements of La and Ga [38, 50-51] to  
493 the Mg-Al-Zn base alloy. The volume fraction of second-phase particles in the SEM  
494 micrograph of the as-cast alloy was 7.3% (Fig. 11c). After the solid-solution treatment  
495 at 693 K (420 °C) for 24 h, the  $\text{Mg}_{17}\text{Al}_{12}$  phase with a melting point of 701 K (437 °C)  
496 [40] disappeared due to its dissolution into the Mg matrix. The volume fraction of  
497 second-phase particles decreased significantly to 2.1% (Fig. 11d). During the heat  
498 treatment, the as-cast dendritic structure changed to an equiaxed grain structure; the  
499 mean grain size determined by using the linear intercept method [52] was  $165 (\pm 5)$   
500  $\mu\text{m}$  (Fig. 11b).



501



502



503

504

505 Fig. 11. Microstructures of the Mg-Al-Zn-RE alloy: (a) dendritic structure of the as-cast alloy; (b)  
 506 equiaxed grain structure of the solid-solution-treated alloy; (c) SEM micrograph of the as-cast  
 507 alloy; (d) SEM micrograph of the solid-solution treated alloy; (e-h) EDS element maps of  $\text{Al}_2\text{Gd}$ ,  
 508  $\text{Al}_{11}\text{La}_3$ ,  $\text{Mg}_{17}\text{Al}_{12}$  and  $\text{Al}_8\text{Mn}_5$  phases.

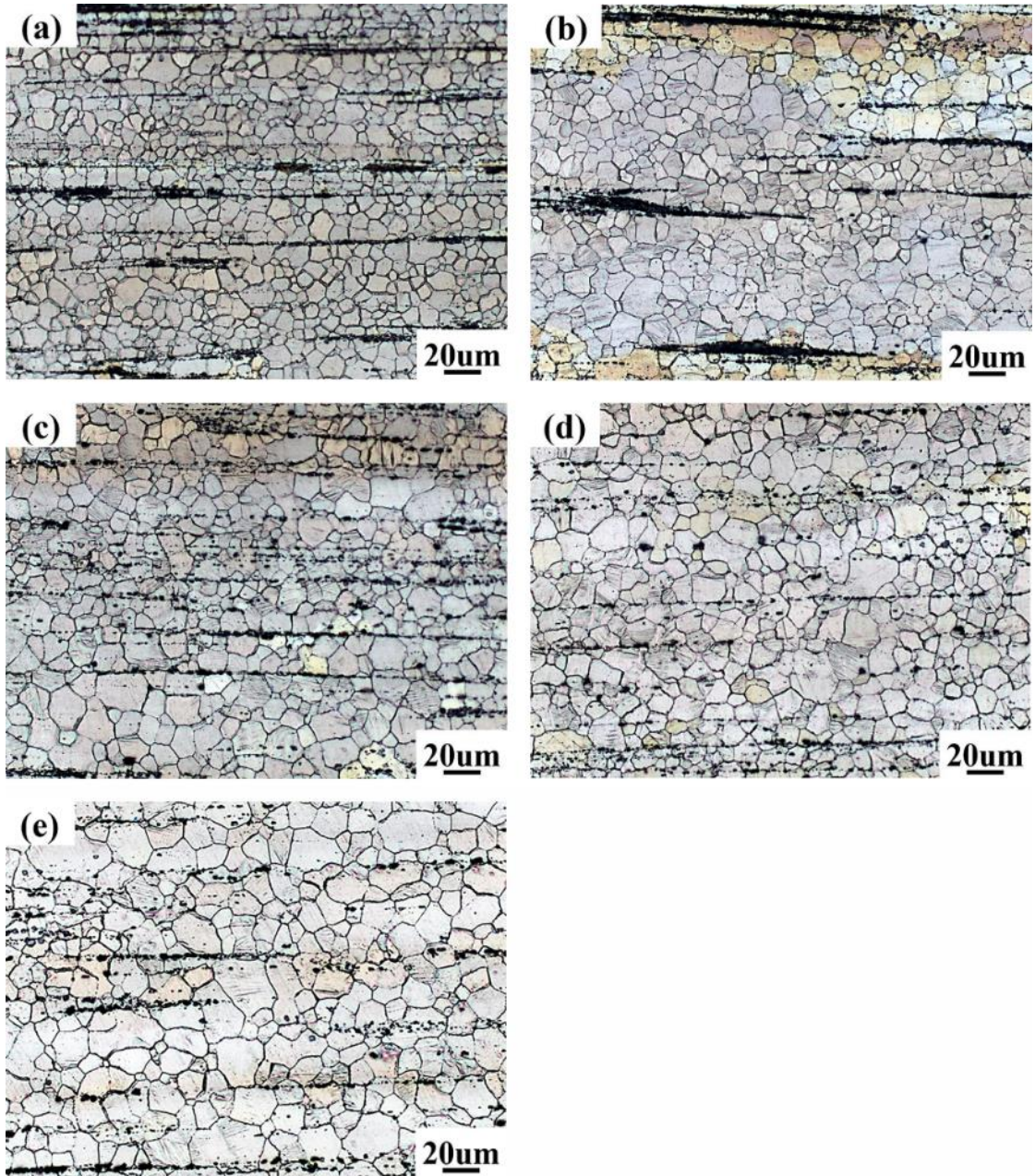
509

Table 4. EDS analysis of second-phase particles in the as-cast alloy.

Phases	$\text{Al}_2\text{Gd}$	$\text{Al}_{11}\text{La}_3$	$\text{Mg}_{17}\text{Al}_{12}$	$\text{Al}_8\text{Mn}_5$
Mg (at. %)		49.84	69.06	1.99
Al (at. %)	68.08	37.25	29.24	64.92
Zn (at. %)		0.78	1.70	
Mn (at. %)		0.41		25.70
La (at. %)	2.90	9.58		
Gd (at. %)	29.03	2.14		6.62

510

511 The optical microstructures of the magnesium alloy rods extruded at temperatures of  
512 523-713 K (250-440 °C), a reduction ratio of 29.8 and stem speed of 3.93 mm/s are  
513 shown in Fig. 12. Apparently, dynamic recrystallization (DRX) occurred during  
514 extrusion under these conditions, and the mean grain sizes of the extruded magnesium  
515 alloy rods reduced significantly from the mean value of the as-solid-solution-treated  
516 alloy. The mean grain sizes of the rods extruded at 523, 573, 623, 673, 673 and 713 K  
517 (250, 300, 350, 400 and 440 °C) were 8.0 ( $\pm 0.3$ ), 8.5 ( $\pm 0.5$ ), 9.5 ( $\pm 0.3$ ), 10.9 ( $\pm$   
518 0.3) and 12.4 ( $\pm 0.4$ )  $\mu\text{m}$ , respectively, showing an increasing trend with rising initial  
519 billet temperature.



520

521

522

523

524

525

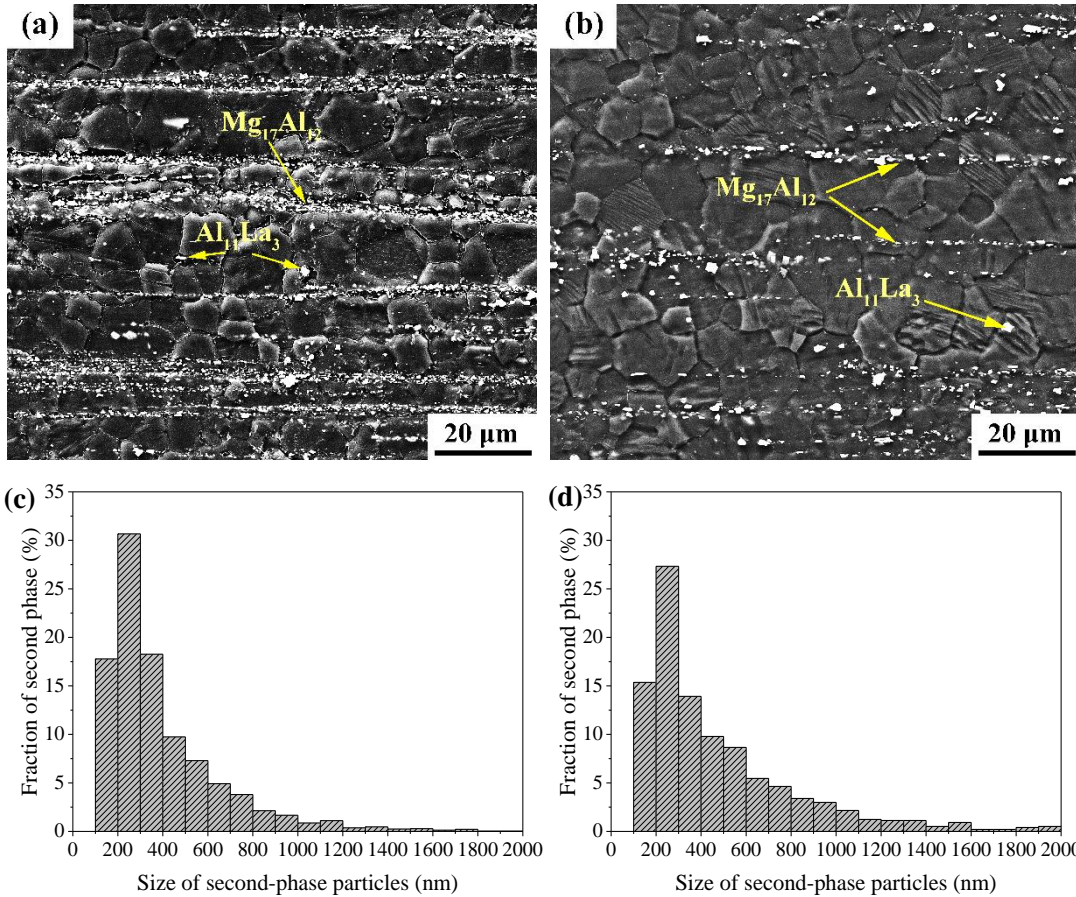
526

Fig. 12. Optical micrographs of the magnesium alloy rods extruded at a reduction ratio of 29.8, stem speed of 3.93 mm/s and initial billet temperatures of (a) 523, (b) 573, (c) 623, (d) 673 and (e) 713 K [(a) 250, (b) 300, (c) 350, (d) 400 and (e) 440 °C].

The second phase  $Mg_{17}Al_{12}$  reappeared due to dynamic precipitation from the supersaturated magnesium solid solution during extrusion and became distributed

527 along the extrusion direction (Fig. 13). The needle-like or lamellar phase  $Al_{11}La_3$  in  
528 the as-solid-solution-treated alloy was broken up and became block-shaped particles  
529 during extrusion. The sizes of second-phase particles increased, but their volume  
530 fraction decreased with increasing initial billet temperature. At the initial billet  
531 temperature of 523 K (250 °C), the maximum temperature of the extrudate reached  
532 702 K (429 °C) and a lot of fine second-phase particles with sizes smaller than 1,000  
533 nm were distributed on recrystallized grain boundaries (Figs. 13a and c). The mean  
534 size of second-phase particles was 397 nm, and the volume fraction was 5.4%. At an  
535 increased initial billet temperature of 623 K (350 °C), the maximum temperature of  
536 the extrudate increased to 749 K (476 °C), the volume fraction of second-phase  
537 particles with sizes of 1,000 nm and larger increased and the mean size of  
538 second-phase particles increased to 492 nm. However, the overall volume fraction of  
539 second-phase particles decreased to 2.8% (Figs. 13b and d) as a result of higher  
540 solubility of the alloying elements in the magnesium matrix at a higher temperature.  
541 This phenomenon also was found in other magnesium alloys with high Al contents  
542 during extrusion [53, 54]. In addition to the dissolution of small particles, the alloying  
543 elements diffused and became accumulated at existing, larger particles, which resulted  
544 in particle growth.

545



546

547

548

549 Fig. 13. SEM micrographs and distributions of the sizes of second-phases particles in the rods

550 extruded at a reduction ratio of 29.8, stem speed of 3.93 mm/s and initial billet temperatures of (a)

551 (c) 523 K (250 °C) and (b) (d) 623 K (350 °C).

552

553 Fig. 14 shows the optical micrographs of the magnesium alloy rods extruded at a

554 billet temperature of 623 K (350 °C), reduction ratio of 29.8 and different stem speeds.

555 With increases in stem speed from 0.96 to 1.92, 3.93, 6.48 and 8.24 mm/s, the mean

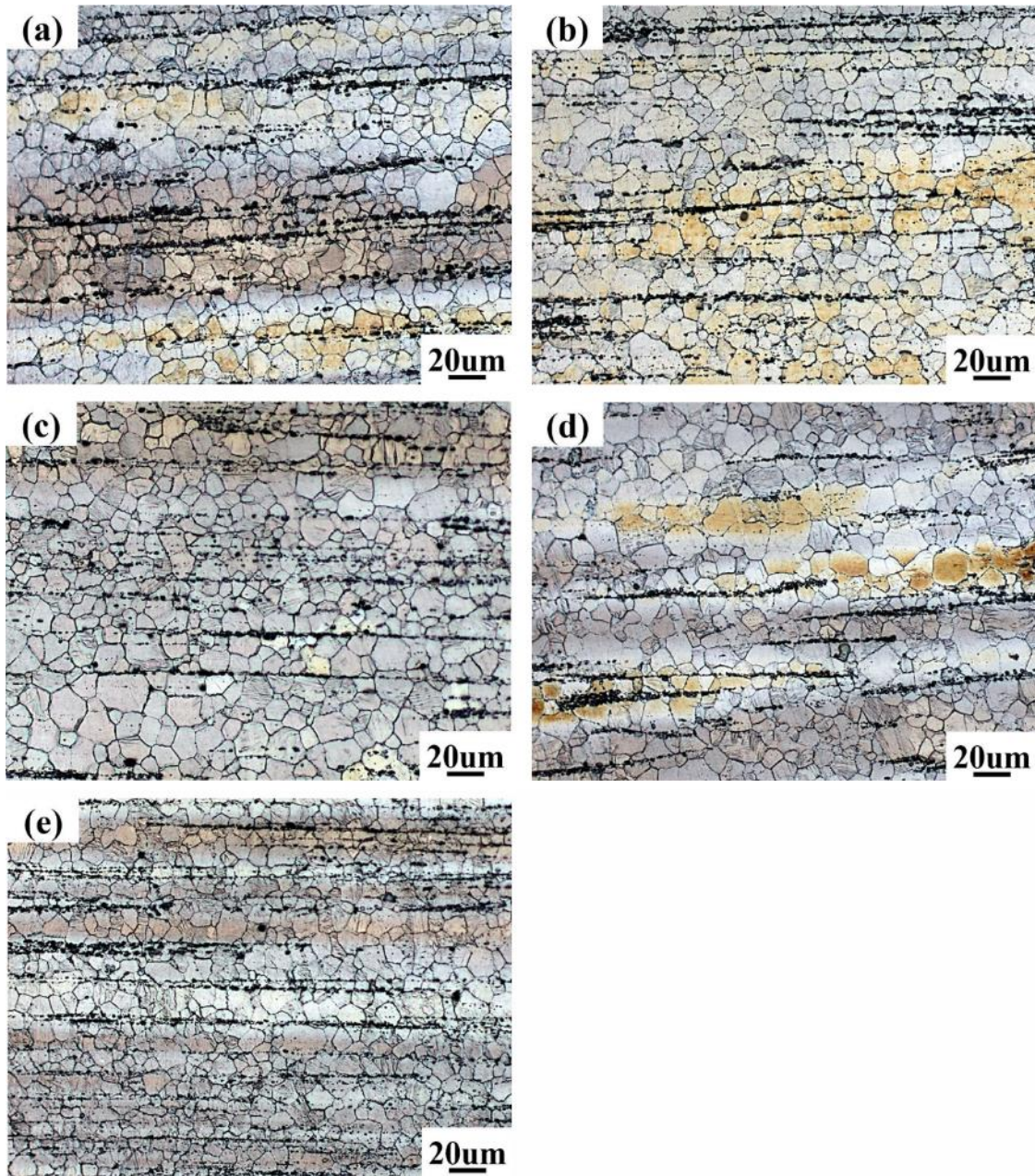
556 grain sizes of the extruded magnesium rods rose marginally from 8.6 ( $\pm 0.5$ ) to 8.9

557 ( $\pm 0.4$ ), 9.5 ( $\pm 0.3$ ), 9.8 ( $\pm 0.6$ ) and 10.1 (0.5)  $\mu m$ , respectively. On the one hand, the

558 extrudate temperature increased with increasing extrusion speed; the maximum

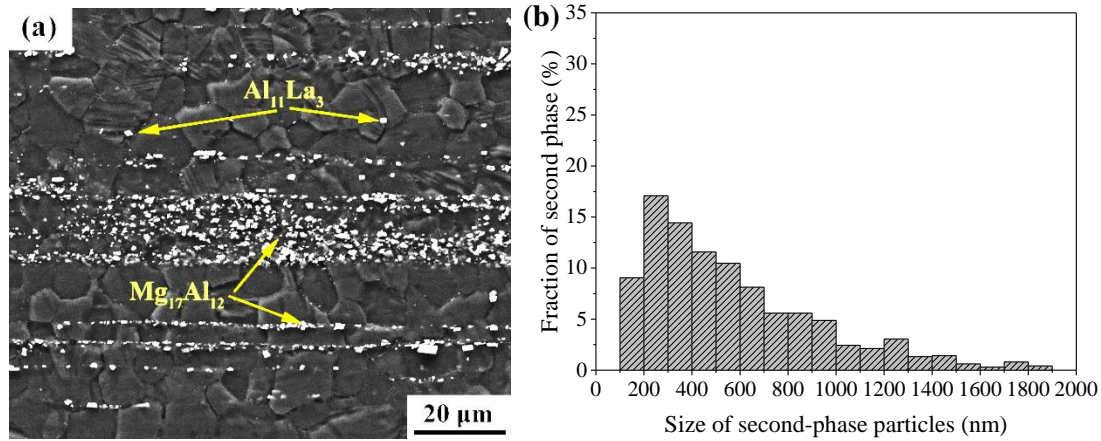
559 extrudate temperature reached 674-787 K (401-514 °C) when stem speed increased  
560 from 0.96 to 8.24 mm/s (Fig. 6b). A high extrudate temperature would normally  
561 promote the growth of DRX grains. But on the other hand, the equivalent strain rate  
562 increased with increasing extrusion speed and a high strain rate would contribute to  
563 grain refinement during the hot deformation of magnesium alloys [55]. In addition,  
564 with increasing extrusion speed, the sizes and volume fraction of second-phase  
565 particles changed, which would affect grain sizes. Fig. 15 presents an SEM  
566 micrograph and a size distribution of second-phase particles in the magnesium alloy  
567 rod extruded at a reduction ratio of 29.8, initial billet temperature of 623 K (350 °C)  
568 and stem speed of 0.96 mm/s. The data could be compared with those obtained from  
569 the magnesium rod extruded at a higher stem speed of 3.93 mm/s, but at the same  
570 reduction ratio and initial billet temperature (Figs. 13b and d). With an increase in  
571 stem speed from 0.96 to 3.93 mm/s, the volume fraction of second-phase particles  
572 decreased from 3.6% to 2.8%, and the mean size decreased from 577 to 492 nm. The  
573 maximum extrudate temperature at stem speeds of 0.96 mm/s and 3.93 mm/s rose to  
574 674 K to 745 K (401 °C and 472 °C), respectively. Clearly, it was the lower extrudate  
575 temperature at a lower extrusion speed that resulted in more and larger dynamically  
576 precipitated second-phase particles, as a result of longer time given for particle  
577 precipitation and growth. Comparison between Fig. 13d and Fig. 15b showed large  
578 volume fractions of second-phase particles smaller than 400 nm in the rods extruded

579 at a higher extrusion speed, which would be highly effective to pin grain boundaries  
580 to retard grain growth.



581  
582 Fig. 14. Optical micrographs of the magnesium alloy rods extruded at a reduction ratio of 29.8,  
583 initial billet temperature of 623 K (350 °C) and stem speeds of (a) 0.96, (b) 1.92, (c) 3.93, (d) 6.48  
584 and (e) 8.24 mm/s.

585



586

587 Fig. 15 SEM micrograph (a) and distribution of the size of second-phase particles (b) in the rods

588 extruded at a reduction ratio of 29.8, stem speed of 0.96 mm/s and initial billet temperature of 623

589 K (350 °C).

590

591 The micrographs of the alloy extruded at the high reduction ratio of 51.0, presented in

592 Fig. 16, were used to analyze the effect of reduction ratio on the microstructure of the

593 extruded alloy. The initial billet temperature was 623 K (350 °C) and the stem speed

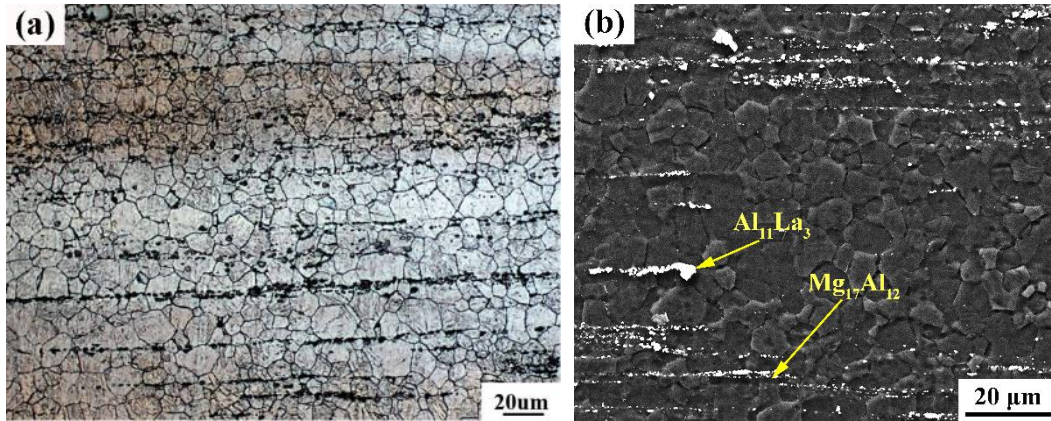
594 was 0.96 mm/s. Comparison of the mean grain size obtained from Fig. 16a with that

595 from Fig. 14a indicated a mild effect of reduction ratio from 29.8 to 51.0 on the mean

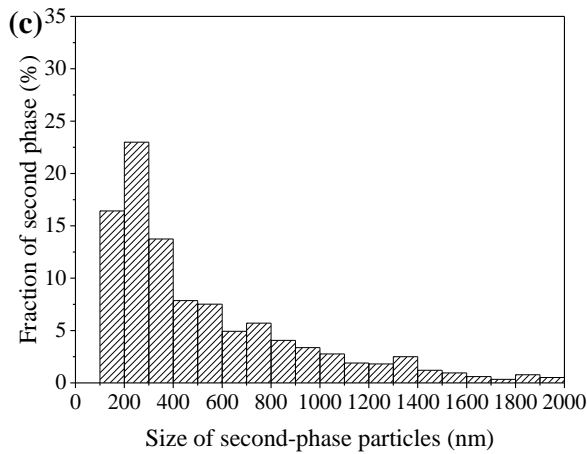
596 grain size (from 8.6 to 9.4 μm). In addition, after extrusion at reduction ratios of 29.8

597 and 51.0, the volume fractions of second-phase particles were 3.6% and 2.9%,

598 respectively, as a result of an increase in extrudate temperature.



599

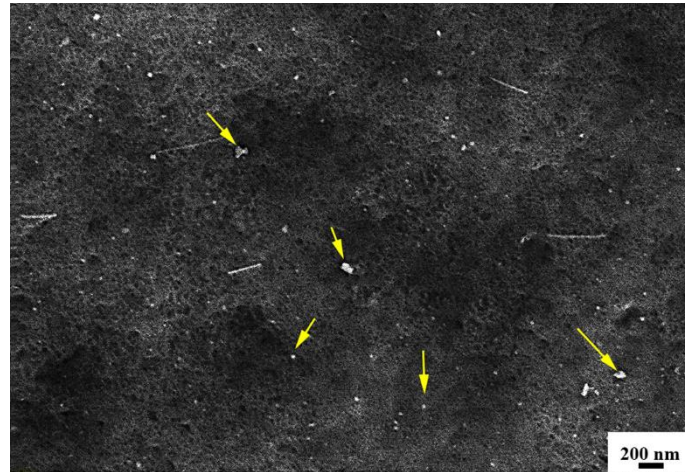


600

601 Fig. 16. Microstructures of the magnesium alloy rods extruded at an initial billet temperature of  
 602 623 K (350 °C), stem speed of 0.96 mm/s and reduction ratio of 51.0: (a) optical micrograph; (b)  
 603 SEM micrograph; (c) distribution of the sizes of second-phase particles.

604 The size distributions and volume fractions of second-phase particles in Figs. 13, 15  
 605 and 16 were determined by using the software Image-Pro Plus on the basis of SEM  
 606 micrographs at 2,000X magnification. With this method, nanoscale particles in the  
 607 range of 1 and 100 nm were ignored, due to too low resolution. Fig. 17 presents a  
 608 SEM micrograph at 20,000X magnification. The observed sample was extruded at an  
 609 initial billet temperature of 623 K (250 °C), extrusion speed of 3.93 mm/s and a  
 610 reduction ratio of 29.8. Nanoscale particles between 1 and 100 nm marked with

611 arrows are clearly discernible. These tiny particles must have contributed to the  
612 improved strength of the extruded magnesium alloy as well, owing to precipitation  
613 strengthening.



614  
615 Fig. 17 SEM micrograph (20,000X) of the magnesium alloy rod extruded at an initial billet  
616 temperature of 523 K (250 °C), extrusion speed of 3.93 mm/s and a reduction ratio of 29.8.

617  
618 In the present research, the mean grain sizes of the magnesium rods extruded under all  
619 the conditions ranged from 7 to 14  $\mu\text{m}$ . The extrusion condition could influence the  
620 mean grain size of the magnesium alloy Mg-Al-Zn-RE to a certain extent, but the  
621 influence was quite moderate, in comparison with other magnesium alloys with low  
622 alloying contents. Zhang et al. [31], for example, reported that at a reduction ratio of  
623 16 and extrusion speed of 4 mm/s, with an increase in billet temperature from 603 K  
624 to 673 K (330 °C to 400 °C), the mean grain size of the extruded Mg-1.0Zn-0.5Ca  
625 alloy increased from 2.5  $\mu\text{m}$  to 25  $\mu\text{m}$ . The main mechanism governing grain  
626 refinement during the hot deformation of a magnesium alloy is dynamic  
627 recrystallization (DRX), including the continuous DRX (CDRX) and discontinuous

628 DRX (DDRX) [55, 56]. DDRX, involving the nucleation and growth of new grains,  
629 was found to be the predominant mechanism in the magnesium alloy AZ31 [57].  
630 Wang et al. [58] demonstrated that a larger value of the Zener-Hollomon parameter  
631 resulted in a higher ratio of nucleation rate to growth rate of new grains in the  
632 magnesium alloy ZM21, which was helpful for grain refinement. For these  
633 magnesium alloys with relatively low alloying contents, extrusion condition was  
634 found to influence the grain size of the extrudate strongly.

635

636 For the present magnesium alloy, abundant precipitates were present due to high  
637 contents of alloying elements added to magnesium. In addition to extrusion condition,  
638 precipitates would influence the DRX behavior of the alloy during extrusion. The  
639 precipitated  $Mg_{17}Al_{12}$  phase and crushed  $Al_{11}La_3$  phase would promote  
640 particle-stimulated nucleation (PSN) for DRX. These phases were mostly distributed  
641 on grain boundaries to exert the Smith-Zener pinning effect and restrict the growth of  
642 DRX grains [38]. Robson et al. [59] demonstrated that coarse, hard second-phase  
643 particles in Mg-Mn alloys, which promoted rapid sub-boundary migration during  
644 deformation, were necessary for the subsequent occurrence of PSN. Deng et al. [60]  
645 found that SiC particles of larger sizes (in the micrometer range) were more effective  
646 in promoting PSN of AZ91-SiC composites and refining grains than SiC particles of  
647 smaller sizes (in the sub-micrometer range). In the present investigation, second-phase  
648 particle sizes increased with increasing initial billet temperature and DRX via PSN

649 would be more important. However, a higher temperature would weaken the  
650 nucleation via DDRX. The competition between these two effects made the mean  
651 grain size of the present alloy appear to be less sensitive to the initial billet  
652 temperature than that of the magnesium alloy Mg-1.0Zn-0.5Ca with low alloying  
653 contents [31].

654

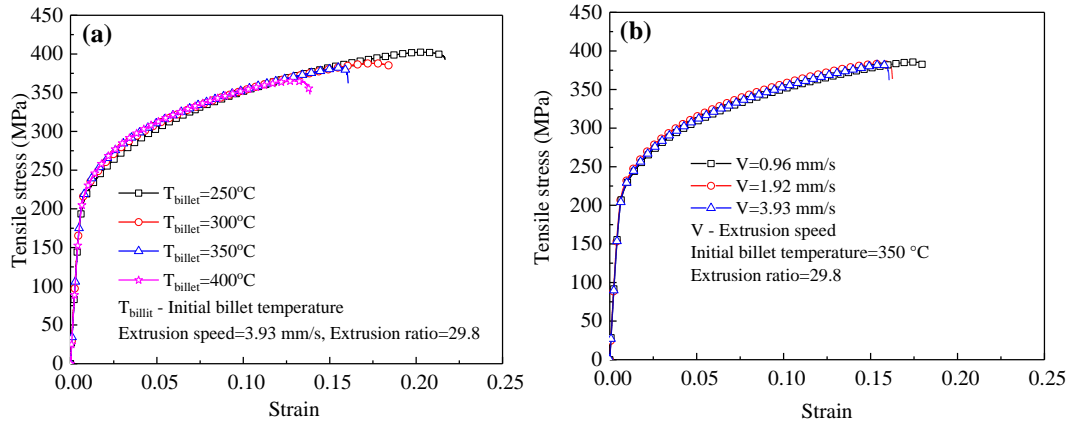
655 As reported earlier, extrusion speed appeared to have a mild influence on the mean  
656 grain size of the present magnesium alloy. With increasing extrusion speed, the strain  
657 rate of the deforming billet and the extrudate temperature increased. A higher  
658 extrudate temperature would promote DRX grain growth, while a high strain rate  
659 would restrain DRX grain growth by increasing nucleation rates. As a net result, the  
660 direct influence of extrusion speed on the mean grain size became nearly invisible.

661

### 662 **3.4 Mechanical properties**

663 Fig. 18 shows the tensile stress-strain curves of the magnesium alloy rods extruded at  
664 different initial billet temperatures and extrusion speeds. Table 5 lists the tensile  
665 properties of the magnesium rods extruded at a reduction ratio of 29.8, together with  
666 mean grain sizes. After extrusion at initial billet temperatures of 523, 573, 623 and  
667 673 K (250, 300, 350 and 400 °C) and a given stem speed of 3.93 mm/s, the extruded  
668 rods had ultimate tensile strengths (UTSs) of  $397 \pm 7$ ,  $387 \pm 1$ ,  $384 \pm 3$  and  $367 \pm 7$   
669 MPa, 0.2% offset yield strengths (YSs) of  $217 \pm 3$ ,  $220 \pm 5$ ,  $221 \pm 1$  and  $221 \pm 6$  MPa,

670 and elongation values of  $20.8 \pm 1.3\%$ ,  $18.2 \pm 0.4\%$ ,  $15.8 \pm 0.4\%$  and  $13.6 \pm 0.4\%$ ,  
671 respectively. Clearly, both the UTS and the elongation decreased with rising initial  
672 billet temperature, which could be attributed to finer DRX grains at a lower initial  
673 billet temperature (Fig. 12 and Table 5). Precipitation strengthening, solid-solution  
674 strengthening, dislocation strengthening and subgrain strengthening might have  
675 contributed to the strength of the material extruded at a low temperature in addition to  
676 fine grain strengthening [38].  
677  
678 YS, UTS and elongation were only slightly improved by extrusion at a lower  
679 extrusion speed. At a given initial billet temperature of 623 K (350 °C), the material  
680 extruded at stem speeds of 0.96, 1.92 and 3.93 mm/s had the UTS values of  $387 \pm 1$ ,  
681  $386 \pm 4$  and  $384 \pm 3$  MPa, the YS values of  $226 \pm 4$ ,  $225 \pm 8$  and  $221 \pm 1$  MPa, and  
682 elongation values of  $17.0 \pm 1.4\%$ ,  $16.6 \pm 0.5\%$  and  $15.8 \pm 0.4\%$ , respectively (Table 5).  
683 The trends were consistent with the trend of the mean grain size varying with  
684 extrusion speed. It means that the scope to control the mean grain size and mechanical  
685 properties by varying extrusion speed appeared to be quite limited, which would give  
686 freedom to choosing extrusion speed for a higher production rate with only a little  
687 effect on the mechanical properties.  
688



689  
690  
691  
692

Fig. 18. Tensile stress-strain curves of the magnesium alloy rods extruded (a) at different billet temperatures and (b) at different extrusion speeds.

693 Table 5. Mechanical properties of the rods extruded at a reduction ratio of 29.8.

Stem speed (mm/s)	Billet temperature (°C)	UTS (MPa)	YS (MPa)	Elongation (%)	Mean grain size (μm)
3.93	250	397 ± 7	217 ± 3	20.8 ± 1.3	8.0 ± 0.3
	300	387 ± 1	220 ± 5	18.2 ± 0.4	8.5 ± 0.5
	350	384 ± 3	221 ± 1	15.8 ± 0.4	9.5 ± 0.3
	400	367 ± 7	221 ± 6	13.6 ± 0.4	10.9 ± 0.3
1.92	350	386 ± 4	225 ± 8	16.6 ± 0.5	8.9 ± 0.4
0.96	350	387 ± 1	226 ± 4	17.0 ± 1.4	8.6 ± 0.5

694

695 The ultimate tensile strengths (UTS), yield strengths (YSs) and mean grain sizes of  
696 selected Mg alloys are listed in Table 6 for comparison. It can be seen that the present  
697 alloy has a mean grain size similar to the mean grain sizes of the magnesium alloys  
698 AZ80 [34] and AZ80-1.52La-1.10Gd [61]. However, the present alloy has a higher  
699 UTS value than the other magnesium alloys of similar compositions. First of all, an  
700 optimized extrusion condition (reduction ratio: 29.8, initial billet temperature: 523 K

701 (250 °C) and ram speed: 3.93 mm/s) was employed to extrude the present alloy.  
702 Moreover, the addition of the rare earth elements raises the strengths of magnesium  
703 alloys. For example, Jiang et al. [50] found that over a Gd content range of 0.3% to  
704 4%, the magnesium alloy AZ80 added with 0.9% Gd exhibited optimum mechanical  
705 properties. This was because coarse second phase particles were formed when  
706 excessive Gd was added to the magnesium alloy, thereby becoming detrimental to the  
707 mechanical properties. Over all, the magnesium alloy with high mechanical properties,  
708 both in UTS, YS and elongation, were obtained through adding rare earth elements to  
709 AZ80 and extrusion at the optimized condition.

710

711 Magnesium alloys with even finer grains and higher mechanical properties can be  
712 prepared through severe plastic deformation (SPD) [62, 63]. For example, Razavi et al.  
713 [63] demonstrated that via the multi-temperature (398 K to 473 K, i.e., 125 °C to  
714 200 °C) equal-channel angular processing (ECAP) the magnesium alloy AZ31  
715 exhibited extraordinarily high mechanical properties (YS =  $385 \pm 6$  MPa, UTS =  $455 \pm$   
716  $4$  MPa, elongation = 12.7%), owing to the ultra-fine grains (mean grain size =  $0.35 \pm$   
717  $0.10$   $\mu\text{m}$ ) formed during SPD. While the SPD process can significantly improve the  
718 mechanical properties of magnesium alloys, this process is only suitable for  
719 small-scale material preparation. With the industrial application taken into  
720 consideration, the commercial extrusion process may be more advantageous than the  
721 SPD process.

722

723

724 Table 6. Yield strengths, ultimate tensile strengths and mean grain sizes of selected

725

Mg alloys for comparison.

Alloy (wt%)	UTS (MPa)	YS (MPa)	Mean grain size ( $\mu\text{m}$ )	Extrusion condition		
				Reduction ratio	Initial billet temperature ( $^{\circ}\text{C}$ )	Ram speed (mm/s)
AZ80 [34]	317-328	200-225	6-8	44	250-350	1
AZ80-1.52La-1.10Gd [61]	304-311	180-225	8.2-13.1	33.6	240-380	2
Mg-3Al-1Zn [63] *	455 $\pm$ 4	385 $\pm$ 6	0.35 $\pm$ 0.10	-	-	-
AZ80-0.2Y-0.2Gd-0.1La [64]	306	264	12 $\pm$ 2	10	380	-
AZ80-1.2Gd-0.8Nd [65]	325	262	-	10	-	-
AZ91-1Ca-0.5Si-0.1La-0.1Ce [66]	318	278	3	30	360	1.45
AZ91-0.3La [67]	330	180	-	17.4	350	1.7
Mg [68]	165	71	33	16.4	350	1.83
Mg-0.2Ce [68]	200-210	-	8	16.4	350	1.83
Mg-3Al [68]	226	105	23	16.4	350	1.83
AZ31 [69]	247	203	23	-	370	-
AM-EX1 [69]	259	184	7	-	370	-
Mg-(0.88-0.96) Mn-(0.32-2.11) Sr [70]	220-250	140-210	35-45	7	350	8
Present alloy (AZ80-1La-0.5Gd)	397 $\pm$ 7	217 $\pm$ 3	8.0 $\pm$ 0.3	29.8	250	3.93

726

\* The values were achieved through severe plastic deformation.

727

728 **4. Conclusions**

729

The extrudability and the effects of extrusion process parameters on the

730

microstructure and mechanical properties of a new Mg-Al-Zn-RE alloy with large

731

amounts of alloying elements were investigated by means of extrusion experiments

732

and FE simulations. The following conclusions could be drawn.

733 (1) Hot shortness was the main defect negatively affecting the surface quality  
734 of the extruded magnesium alloy. The tendency for hot shortness to occur increased  
735 with increasing initial billet temperature, extrusion speed and reduction ratio. The  
736 critical temperature for hot shortness to occur was found to be between 754 K and 768  
737 K (481 °C and 495 °C).

738 (2) DRX occurred during hot extrusion and grains were significantly refined.  
739 The mean grain size of the extruded alloy decreased with decreasing initial billet  
740 temperature. An increase in extrusion speed and reduction ratio only slightly  
741 promoted DRX grain growth. Fine grains with a mean size of  $8.0 (\pm 0.3) \mu\text{m}$  were  
742 present in the alloy extruded at an initial billet temperature of 523 K (250 °C), stem  
743 speed of 3.93 mm/s and reduction ratio of 29.8.

744 (3) The  $\text{Mg}_{17}\text{Al}_{12}$  phase dynamically precipitated during extrusion from the  
745 supersaturated magnesium matrix after the solid solution treatment. The  $\text{Al}_{11}\text{La}_3$  phase  
746 was crushed during extrusion. A large number of second-phase particles with sizes  
747 smaller than  $1.0 \mu\text{m}$  were distributed on grain boundaries. The volume fraction of  
748 second-phase particles decreased with rising extrudate temperature. These particles  
749 aided in DRX grain refinement through particle-stimulated nucleation and grain  
750 boundary pinning.

751 (4) The UTS and elongation of the extruded rod increased with decreasing initial  
752 billet temperature and extrusion speed. The extruded rod with an optimum  
753 combination of mechanical properties ( $\text{YS}=217 \pm 3 \text{ MPa}$ ,  $\text{UTS}=397 \pm 7 \text{ MPa}$  and

754 elongation=20.8% ( $\pm 1.3\%$ ) was obtained at an initial billet temperature of 523 K  
755 (250 °C), stem speed of 3.93 mm/s and reduction ratio of 29.8 mainly as a result of a  
756 refined grain structure.

757

## 758 **Acknowledgements**

759 The authors (Gang Fang and Sheng-Wen Bai) greatly appreciate the financial support  
760 of the National Natural Science Foundation of China (Project No.51675300).

761

## 762 **References**

- 763 [1] M.K. Kulekci, Int. J. Adv. Manuf. Tech., 2008, vol. 39, pp. 851-865.
- 764 [2] A.A. Luo, Int. Mater. Rev., 2004, vol. 49, pp. 13-30.
- 765 [3] E.F. Volkova, Met. Sci. Heat Treat., 2006, vol. 48, pp. 473-478
- 766 [4] S. Yao, Y.F. Li, Sci. Total Environ., 2015, vol. 44, pp. 89-96.
- 767 [5] H. Pan, Y. Ren, H. Fu, H. Zhao, L. Wang, X. Meng, G. Qin, J. Alloy. Compd., 2016,  
768 vol. 663, pp. 321-331.
- 769 [6] D. Letzig, J. Swiostek, J. Bohlen, P. A. Beaven, K.U. Kainer, Metal Science J.,  
770 2013, vol. 24, pp. 991-996.
- 771 [7] A.A. Luo, J. Magn. Alloy., 2013, vol. 1, pp. 2-22.

- 772 [8] W. A. Monteiro, S. J. Buso, L. V. da Silva, Application of magnesium alloys in  
773 transport, in: W.A. Monteiro (Ed.), *New Features on Magnesium Alloys*, InTech,  
774 Rijeka, 2012, pp. 1-14.
- 775 [9] S. You, Y. Huang, K.U. Kainer, N. Hort, *J. Magn. Alloys*, 2017, vol. 5, pp.  
776 239-253.
- 777 [10]Z. Zeng, N. Stanford, C.H.J. Davies, J.F. Nie, N. Birbilis, *Int. Mater. Rev.*, 2018,  
778 vol. 2, pp. 1-36.
- 779 [11]C. Bettles, M. Barnett, *Advances in Wrought Magnesium Alloys: Fundamentals of*  
780 *Processing, Properties and Applications*, Woodhead Publishing, Philadelphia, PA,  
781 USA, 2012, pp. 304-322.
- 782 [12]D.S. Yin, E.L. Zhang, S.Y. Zeng, *Trans. Nonferr Metal. Soc.*, 2008, vol. 18, pp.  
783 763-768.
- 784 [13]W.N. Tang, S.S. Park, B.S. You, *Mater. Des.*, 2011, vol. 32, pp. 3537-3543.
- 785 [14]S. M. Masoudpanah, R. Mahmudi, *Mater. Sci. Eng.*, 2009, vol. A526, pp. 22-30.
- 786 [15]B. Zhang, Y. Wang, L. Geng, C. Lu, *Mater. Sci. Eng. A*, 2012, vol. 539, pp. 56-60.
- 787 [16]J. Bohlen, S. Yi, D. Letzig, K.U. Kainer, *Mater. Sci. Eng. A*, 2010, vol. 527, pp.  
788 7092-7098.
- 789 [17]D.K. Xu, W.N. Tang, L. Liu, Y.B. Xu, E.H. Han, *J. Alloy. Compd.*, 2007, vol. 432,  
790 pp. 129-134.
- 791 [18]D.K. Xu, L. Liu, Y.B. Xu, E.H. Han, *J. Alloy. Compd.*, 2006, vol. 426, pp. 155-161.
- 792 [19]N. Stanford, M. R. Barnett, *Mater. Sci. Eng. A*, 2008, vol. 496, pp. 399-408.

- 793 [20]M. Yamasaki, K. Hashimoto, K. Hagihara, Y. Kawamura, *Acta Mater.*, 2011, vol.  
794 59, pp. 3646-3658.
- 795 [21]X. Li, W. Qi, K. Zheng, N. Zhou, *J. Magn. Alloys*, 2013, vol. 1, pp. 54-63.
- 796 [22]X. Zeng, Y. Zhang, C. Lu, W. Ding, Y. Wang, Y. Zhu, *J. Alloy. Compd.*, 2005, vol.  
797 395, pp. 213-219.
- 798 [23]N. Stanford, D. Atwell, M. R. Barnett, *Acta Mater.*, 2010, vol. 58, pp. 6773-6783.
- 799 [24]J.B. Zhang, L.B. Tong, C. Xu, Z.H. Jiang, L.R. Cheng, S. Kamado, H.J. Zhang,  
800 *Mater. Sci. Eng. A*, 2017, vol. 708, pp. 11-20.
- 801 [25]T. Homma, N. Kunito, S. Kamado, *Scripta Mater.*, 2009, vol. 61, pp. 644-647.
- 802 [26]M. Yamasaki, T. Anan, S. Yoshimoto, Y. Kawamura, *Scripta Mater.*, 2005, vol. 53,  
803 pp. 799-803.
- 804 [27]Y. Chen, L. Hao, Y. Ruiyu, G. Liu, T. Xia, *Mater. Sci. Technol.*, 2014, vol. 30, pp.  
805 495-500.
- 806 [28]A. A. Luo, C. Zhang, A. K. Sachdev, *Scripta Mater.*, 2012, vol. 66, pp. 491-494.
- 807 [29]T. Murai, S.I. Matsuoka, S. Miyamoto, Y. Oki, *J. Mater. Process. Technol.*, 2001,  
808 vol. 141, pp. 207-212.
- 809 [30]S. Ishihara, H. Shibata, K. Komano, T. Goshima, Z.Y. Nan, *Key Eng. Mater.*, 2007,  
810 vol. 353, pp. 291-294.
- 811 [31]B.P. Zhang, L. Geng, L.J. Huang, X.X Zhang, C.C. Dong, *Scripta Mater.*, 2010, vol.  
812 63, pp. 1024-1027.

- 813 [32]L.B. Tong, M.Y. Zheng, L.R. Cheng, D.P. Zhang, S. Kamado, J. Meng, H.J. Zhang,  
814 Mater. Charact., 2015, vol. 104, pp. 66-72.
- 815 [33]S.H. Park, J.G. Jung, Y.M. Kim, B.S. You, Mater. Lett., 2015, vol. 139, pp. 35-38.
- 816 [34]M. Shahzad, L. Wagner, Mater. Sci. Eng. A, 2009, vol. 506, pp. 141-147.
- 817 [35]Q. Chen, D. Shu, Z. Zhao, Z. Zhao, Y. Wang, B. Yuan, Mater. Des., 2012, vol. 40,  
818 pp. 488-496.
- 819 [36]A. Singh, Y. Osawa, H. Somekawa, H. Somekawa, T. Mukai, C.J. Parrish, D.S.  
820 Shih, Metall. Mater. Trans. A, 2014, vol. 45, pp. 3232-3240.
- 821 [37]S.H. Park, J.H. Bae, S.H. Kim, J. Yoon, B.S. You, Metall. Mater. Trans. A, 2015,  
822 vol. 46, pp. 5482-5488.
- 823 [38]F. Bu, Q. Yang, K. Guan, X. Qiu, D. Zhang, W. Sun, J. Alloy. Compd., 2016, vol.  
824 688, pp. 1241-1250.
- 825 [39]X. Luo, S. Dang, L. Kang, Adv. Mater. Sci. Eng., 2014, vol. 2014, pp. 1-7.
- 826 [40]J. Mohammadi, M. Ghoreishi, Y. Behnamian, Mater. Res., 2014, vol. 17, pp.  
827 994-1002.
- 828 [41]C.M. Sellars, W.J. McTegart, Acta Metall., 1966, vol. 14, pp. 1136-38
- 829 [42]L. Li, H. Zhang, J. Zhou, J. Duszczyk, G. Li, Z.H. Zhong, Mater. Des., 2008, vol.  
830 29, pp. 1190-1198.
- 831 [43]G. Liu, J. Zhou, J. Duszczyk, J. Mater. Process. Technol., 2008, vol. 200, pp.  
832 185-198.

- 833 [44]L. Li, J. Zhou, and J. Duszczyk, *J. Mater. Process. Technol.*, 2006, vol. 172, pp.  
834 372–80.
- 835 [45]J. Zhou, L. Li, J. Duszczyk, *J. Mater. Process. Technol.*, 2003, vol. 134, pp.  
836 383-397.
- 837 [46]T. Sheppard, *Extrusion of Aluminum Alloys*, Kluwer Academic Publishers,  
838 Dordrecht, The Netherlands, 1999, pp. 227–52.
- 839 [47]M.P. Clade, T. Sheppard, *Mater. Sci. Technol.*, 1993, vol. 9, pp. 313-318.
- 840 [48]W. Wei, C. Xu, J. Zhang, X. Niu, *China Foundry*, 2014, vol. 11, pp. 157-162.
- 841 [49]Y.S. Yang, J.C. Wang, T. Wang, C.M. Liu, Z.M. Zhang, *Trans. Nonferr Metal. Soc.*,  
842 2014, vol. 24, pp. 76-81.
- 843 [50]N. Jiang, L.G. Meng, X.G. Zhang X G, L. Chen, C.F. Fang, H. Hao, *Rare Met.*,  
844 2017, pp. 1-7.
- 845 [51]X.D. Wang, W.B. Du, K. Liu, Z.H. Wang, S.B. Li, *J. Alloys Comp.*, 2012, vol. 522,  
846 pp. 78– 84.
- 847 [52]J.C. Wurst, J.A. Nelson, *J. Am. Ceram. Soc.*, 1972, vol. 55, pp. 109-109.
- 848 [53]H. Ding, L. Liu, S. Kamado, D. Wang, Y. Kojima, *J. Alloy. Compd.*, 2008, vol. 456,  
849 pp. 400-406.
- 850 [54]S.W Xu, N. Matsumoto, S. Kamado, T. Honma, Y. Kojima, *Scripta Mater.*, 2009,  
851 vol. 61, pp. 249-252.
- 852 [55]S.M. Fatemi-Varzaneh, A. Zarei-Hanzaki, H. Beladi, *Mater. Sci. Eng. A*, 2007, vol.  
853 456, pp. 52-57.

- 854 [56]O. Sitdikov, R. Kaibyshev, *Mater. Trans.*, 2001, vol. 42, pp. 1928-1937.
- 855 [57]A.G. Beer, M.R. Barnett, *Metall. Mater. Trans. A*, 2007, vol. 38, pp. 1856-1867.
- 856 [58]L. Wang, G. Fang, L. Qian, *Mater. Sci. Eng. A*, 2018, vol. 711, pp. 268-283.
- 857 [59]J.D. Robson, D.T. Henry, B. Davis, *Acta Mater.*, 2009, vol. 57, pp. 2739-2747.
- 858 [60]K.K. Deng, X.J. Wang, Y.W. Wu, X.S. Hu, K. Wu, W.M. Gan, *Mater. Sci. Eng. A*,  
859 2012, vol. 543, pp. 158-163.
- 860 [61]Q. Liao, X. Chen, Q. Lan, F. Ning, Q. Le, *Mater. Res. Express*, 2018, vol. 5, pp.  
861 1-10.
- 862 [62]D.C. Foley, M. Al-Maharbi, K.T. Hartwig, I. Karaman, L.J. Kecskes, S.N.  
863 Mathaudhu, *Scripta Mater.*, 2011, vol. 64, pp. 193-196.
- 864 [63]S.M. Razavi, D.C. Foley, I. Karaman, K.T. Hartwig, O. Duygulu, L.J. Kecskes,  
865 S.N. Mathaudhu, V.H. Hammond, *Scripta Mater.*, 2012, vol. 67, pp. 439-442.
- 866 [64]K. Cai, Z. Gao, Q. Zhu, Y. Jin, Y. Chai, D. Fang, *Rare Metal Mater. Eng.*, 2015, vol.  
867 44, pp. 1489-1493.
- 868 [65]Q. Zhu, C. Fang, N. Li, L. Meng, Y. Wang, Y. Wu, X. Zhang, *Rare Metal Mater.*  
869 *Eng.*, 2013, vol. 42, pp. 771-775.
- 870 [66]C. Che, Z. Cai, X. Yang, L. Cheng, Y. Du, *Mater. Sci. Eng. A*, 2017, vol. 705, pp.  
871 282-290.
- 872 [67]L. Fu, X.B. Wang, P.L. Gou, Q.C. Le, W. T. Jia, Y. Tang, *Adv. Eng. Mater.*, 2017,  
873 vol. 19, pp. 1700230.

- 874 [68] A.A. Luo, W. Wu, R.K. Mishra, L. Jin, A.K. Sachdev, W. Ding, *Metall. Mater.*  
875 *Trans. A*, 2010, vol. 41, pp. 2662-2674.
- 876 [69] M. Easton, A. Beer, M. Barnett, C. Davies, G. Dunlop, Y. Durandet, S. Blacket, T.  
877 Hilditch, P. Beggs, *JOM*, 2008, vol. 60, pp. 57-62.
- 878 [70] H. Borkar, M. Hoseini, M. Pekguleryuz, *Mater. Sci. Eng. A*, 2012, vol. 549, pp.  
879 168-175.

## 880 **Table and figure captions**

- 881 Table 1. Nominal chemical composition (wt.%) of the Mg-Al-Zn-RE alloy.
- 882 Table 2. Constitutive constants of the magnesium alloy (Mg-Al-Zn-RE).
- 883 Table 3. Physical properties of the billet and extrusion tooling.
- 884 Table 4. EDS analysis of second-phase particles in the as-cast alloy.
- 885 Table 5. Mechanical properties of the rods extruded at a reduction ratio of 29.8.
- 886 Table 6. Yield strengths, ultimate tensile strengths and mean grain sizes of selected  
887 Mg alloys for comparison.
- 888
- 889 Fig. 1. Flow stress curves of the magnesium alloy at temperatures from 773 K to 693  
890 K (300 °C to 420 °C) and strain rates (a) 0.001 s<sup>-1</sup>, (b) 0.01 s<sup>-1</sup>, (c) 0.1 s<sup>-1</sup>, (d) 1 s<sup>-1</sup> and  
891 (e) 10 s<sup>-1</sup>.

892 Fig. 2. Tooling set-up to extrude rods: (a) schematic and (b) dimensions of one of the  
893 extrusion dies.

894 Fig. 3. Schematic of the longitudinal section of an extruded rod for microstructure  
895 observation.

896 Fig. 4. Axisymmetric FE model to simulate the extrusion process to produce rods.

897 Fig. 5. Predicted temperature distribution inside the billet, extrudate and extrusion  
898 tooling (a) and comparison between the measured and predicted temperatures at P1  
899 along with stem displacement (b).

900 Fig. 6. FE simulated temperature evolutions at point P2 during extrusion: (a) at a  
901 reduction ratio of 29.8, stem speed of 3.93 mm/s and different initial billet  
902 temperatures, (b) at a reduction ratio of 29.8, initial billet temperature of 623 K  
903 (350 °C) and different stem speeds, and (c) at a reduction ratio of 51.0, initial billet  
904 temperature of 623 K (350 °C) and different stem speeds.

905 Fig. 7. Simulated temperatures at point P2 with friction factor values of 0 and 1.

906 Fig. 8. Magnesium alloy rods extruded at a reduction ratio of 29.8, stem speed of 3.93  
907 mm/s and different billet temperatures. (a)  $T=523$  K (250 °C) and  $T_e=702$  K (429 °C);  
908 (b)  $T=573$  K (300 °C) and  $T_e=723$  K (450 °C); (c)  $T=623$  K (350 °C) and  $T_e=749$  K  
909 (476 °C); (d)  $T=673$  K (400 °C) and  $T_e=769$  K (496 °C); (e)  $T=713$  K (440 °C) and  
910  $T_e=793$  K (520 °C).  $T_e$  is the maximum extrudate temperature.

911 Fig. 9. Magnesium alloy rods extruded at a reduction ratio of 29.8, initial billet  
912 temperature of 623 K (350 °C) and different stem speeds. (a)  $v=0.96$  mm/s and  
913  $T_e=674$  K (401 °C); (b)  $v=1.92$  mm/s and  $T_e=712$  K (439 °C); (c)  $v=3.93$  mm/s and  
914  $T_e=749$  K (476 °C); (d)  $v=6.48$  mm/s and  $T_e=768$  K (495 °C); (e)  $v=8.24$  mm/s and  
915  $T_e=787$  K (514 °C).  $T_e$  is the maximum extrudate temperature.

916 Fig. 10. Magnesium alloy rods extruded at a reduction ratio of 51.0, initial billet  
917 temperature of 623 K (350 °C) and different stem speeds. (a)  $v=0.96$  mm/s and  
918  $T_e=690$  K (417 °C); (b)  $v=1.92$  mm/s and  $T_e=733$  K (460 °C); (c)  $v=3.07$  mm/s and  
919  $T_e=754$  K (481 °C); (d)  $v=3.93$  mm/s and  $T_e=779$  K (506 °C); (e)  $v=5.39$  mm/s and  
920  $T_e=786$  K (513 °C).  $T_e$  is the maximum extrudate temperature.

921 Fig. 11. Microstructures of the Mg-Al-Zn-RE alloy: (a) dendritic structure of the  
922 as-cast alloy; (b) equiaxed grain structure of the solid-solution-treated alloy; (c) SEM  
923 micrograph of the as-cast alloy; (d) SEM micrograph of the solid-solution treated  
924 alloy; (e-h) EDS element maps of  $Al_2Gd$ ,  $Al_{11}La_3$ ,  $Mg_{17}Al_{12}$  and  $Al_8Mn_5$  phases.

925 Fig. 12. Optical micrographs of the magnesium alloy rods extruded at a reduction  
926 ratio of 29.8, stem speed of 3.93 mm/s and initial billet temperatures of (a) 523, (b)  
927 573, (c) 623, (d) 673 and (e) 713 K [(a) 250, (b) 300, (c) 350, (d) 400 and (e) 440 °C].

928 Fig. 13. SEM micrographs and distributions of the sizes of second-phases particles in  
929 the rods extruded at a reduction ratio of 29.8, stem speed of 3.93 mm/s and initial  
930 billet temperatures of (a) (c) 523 K (250 °C) and (b) (d) 623 K (350 °C).

931 Fig. 14. Optical micrographs of the magnesium alloy rods extruded at a reduction  
932 ratio of 29.8, initial billet temperature of 623 K (350 °C) and stem speeds of (a) 0.96,  
933 (b) 1.92, (c) 3.93, (d) 6.48 and (e) 8.24 mm/s.

934 Fig. 15. SEM micrograph (a) and distribution of the size of second-phase particles (b)  
935 in the rods extruded at a reduction ratio of 29.8, stem speed of 0.96 mm/s and initial  
936 billet temperature of 623 K (350 °C).

937 Fig. 16. Microstructures of the magnesium alloy rods extruded at an initial billet  
938 temperature of 623 K (350 °C), stem speed of 0.96 mm/s and reduction ratio of 51.0:  
939 (a) optical micrograph; (b) SEM micrograph; (c) distribution of the sizes of  
940 second-phase particles.

941 Fig. 17. SEM micrograph (20,000X) of the magnesium alloy rod extruded at an initial  
942 billet temperature of 523 K (250 °C), extrusion speed of 3.93 mm/s and a reduction  
943 ratio of 29.8.

944 Fig. 18. Tensile stress-strain curves of the magnesium alloy rods extruded (a) at  
945 different billet temperatures and (b) at different extrusion speeds.